Stony Brook University

The official electronic file of this thesis or dissertation is maintained by the University Libraries on behalf of The Graduate School at Stony Brook University.

Threading Dislocation Characterization and Stress Mapping Depth Profiling

via Ray Tracing Technique

A Thesis Presented

by

Tianyi Zhou

to

The Graduate School

in Partial Fulfillment of the

Requirements

for the Degree of

Master of Science

in

Materials Science and Engineering

Stony Brook University

May, 2013

Stony Brook University

The Graduate School

Tianyi Zhou

We, the thesis committee for the above candidate for the

Master of Science degree, hereby recommend

acceptance of this thesis.

Michael Dudley – Thesis Advisor
Professor, Department of Materials Science and Engineering

Balaji Raghothamachar– Second Reader
Research Professor, Department of Materials Science and Engineering

T. A. Venkatesh– Third Reader
Assistant Professor, Department of Materials Science and Engineering

This thesis is accepted by the Graduate School

Charles Taber
Interim Dean of the Graduate School

Abstract of the Thesis

Threading Dislocation Characterization and Stress Mapping Depth Profiling

via Ray Tracing Technique

by

Tianyi Zhou

Master of Science

in

Materials Science and Engineering

Stony Brook University

2013

Zinc oxide (ZnO) has been well known as a transparent, dielectric, piezoelectric and wide band gap material. The potential capabilities have been demonstrated for a wide range of applications such as piezoelectric transducer, gas sensor, optical waveguides and transparent electrode. It could also be applied as a substrate material for GaN-based devices. However, while some applications have already been realized, issues relating to crystalline defects remain a barrier to the successful realization of several others. In this thesis, the central focus of Chapter II is to characterize threading dislocations in hydrothermal grown ZnO substrates through simulation work as well as other techniques. The goal of this study is to find the origin of threading dislocations and design strategies to mitigate their negative effects by either reducing their densities or completely eliminating them.

In Chapter III, the technique of SMART (stress mapping analysis via ray tracing) is discussed in detail to measure residue stress in packaged silicon circuits. Residual stress plays an important role in the performance and lifetime of single crystal device material. There are mainly two advantages of SMART compared with other techniques: (a) all six components of the stress tensor could be evaluated; (b) it is non-destructive and no damaging trace will be left on the sample. In this study, our goal is to build a relationship between stress distribution and depth. The concept of penetration depth is critically important in this study and its value may cause great changes for real space stress distribution. A new function is applied to get better fitting curves. Data in this study is obtained from various penetration depth, which represents exponentially decaying weighted average of actual stress value or in other words this stress profile is Laplace transform of real stress profile. Mathematical procedure is described to determine real stress profile from Laplace profile. Experiment procedure, detailed penetration depth calculation, accurate positioning of film and sample and error analysis is introduced in this study.

Table of Contents

List of Figures

List of Tables

List of Abbreviations

BPD   basal plane dislocation

MP   micropipe

PVT   physical vapor transport

SF   stacking fault

SMART   stress mapping via ray tracing

SWBXT   synchrotron white beam x-ray topography

TED   threading edge dislocation

TEM   transmission electron microscope

TSD   threading screw dislocation

XRT   x-ray topography

Acknowledgments

First I would like to give my deep and sincere gratitude to Professor Michael Dudley, my advisor, for providing me this great opportunity to study in the field of characterization simulation and stress analysis. His wide knowledge and helpful guidance have been of great value for me. No doubt his understanding, encouragement and personal guidance have always been providing an excellent basis for my research.

I would like to thank Dr. Balaji Raghothamachar, valuable suggestion and discussion during the entire research project.

I would like to thank Professor T. A. Venkatesh for being in my committee member and his help and suggestion during my research project.

I would also like to thank my colleagues: Mr. Fangzhen Wu, Ms. Huanhuan Wang, Mr. Shayan Byrappa, Ms. Hao Wang, Ms. Shun Sun, Mr. Goue Ouloide Yannick and Ms. Yu Yang for their help and during my research.

I would also like to thank Mr. Guang Chen and Mr. Cong Zhang for help with mathwork and stress analysis.

I would also like to acknowledge continuous help and support of graduate program coordinator Ms. Deborah Michienzi, and Ms. Chandrani Roy.

Finally, I would like to thank my parents Mr. Yan Zhou and Mrs. Guizhen Jiang, for their great assistance during my study. Without them, I would not have been able to spend so much time on my research.

Chapter I. Introduction

1.1 Fundamentals of X-ray Diffraction Topography

X-ray diffraction topography (XRT) has been a powerful non-destructive imaging technique based on Bragg's Law, by the means of X-ray diffraction to identify micrometer-sized and centimeter-sized defects inside crystals and to determine the crystalline structure for over 50 years. An X-ray topographic image is a two dimensional image obtained by projecting the distribution of diffracted intensity in an area-filling diffracted beam, produced by a low-divergence area-filling X-ray beam incident on a single crystal set at the Bragg angle, onto a two dimensional detector. This intensity mapping reflects the distribution of scattering power inside the crystal; topographs therefore reveal the irregularities in a crystal lattice. The technique is not sensitive to the surface topograph; it is the topography of crystal lattice planes that are examined.

X-ray was first found by Wilhelm Röntgen in 1895; and it still took several decades for the benefits of X-ray diffraction images to be fully recognized after Laue and the Braggs family has built the basic principles of X-ray diffraction. Early works by Schulz and Guinier and Tennevin, which mainly recorded the intensity distribution of Laue spots could not tell much information about individual dislocations. Most of these early works rely on characteristic X-rays from laboratory source. The development of synchrotron source has further advanced this technique by enabling white beam topography and enhancing monochromatic X-ray technique.

Kinematical and dynamical theories of X-ray diffraction are employed to explain x-ray diffraction phenomena in crystalline materials. Laue's kinematical theory[1] provides good approximation when X-rays interact with relatively small imperfect crystal, whereas dynamical theory proposed by Ewald and Darwin is useful for large and highly perfect crystal. Nonetheless kinematical theory plays an important role in interpreting topographic contrasts and is discussed latter in this chapter. In the kinematical theory, X-rays are assumed to be scattered by atom only once, and re-scattering is negligible. Dynamical theory considers re-scattering of X-rays in the lattice.

In X-ray topography, the crystal sample is illuminated by an X-ray beam and images of the diffracted beams are recorded. These images are generally formed from X-ray wave fields interfering with one another inside the crystal. The image from a perfect crystal is usually completely homogeneous. Changes in the image contrast are seen if there are imperfections in the crystal which cause deviations from perfect long-range atomic order. In most cases, the defects themselves are not visible in the image, but rather the lattice deformations surrounding the defects are seen. The image contrast mechanism will be discussed later.

In general, there are three geometries in XRT, transmission, back reflection and grazing

geometry for synchrotron white x-ray beam. Grazing Geometry could be view as one kind of reflection in small incident angel. In transmission geometry, x-ray beam passes through the whole crystal and therefore, it reflects the information of bulk material; in grazing geometry, due to its low penetration depth, defect information on the sample surface could be collected. In this study, these two geometries are commonly used.
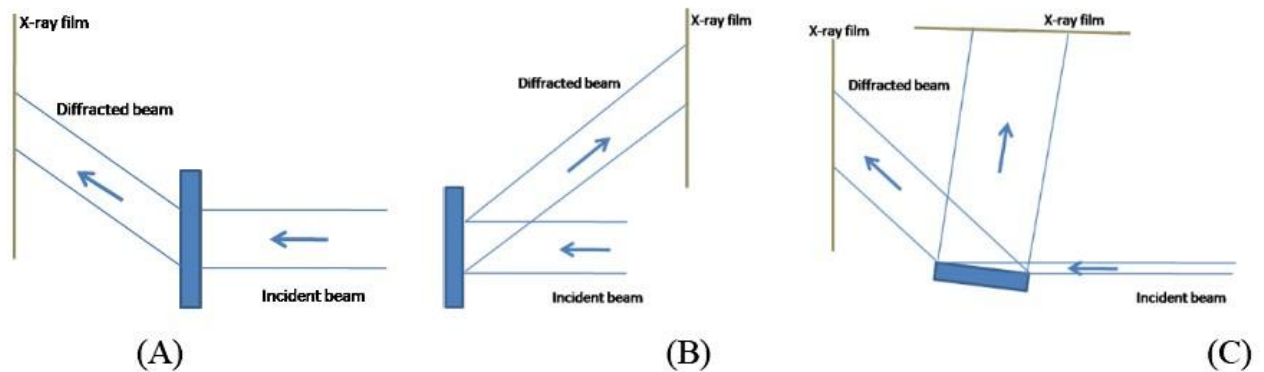
Figure 1: Schematic of three geometries used in XRT, (A) transmission, (B) back reflection and (c) grazing

Synchrotron radiation is especially suitable for x-ray topography because of the high brightness and low divergence of the x-ray beam. The vertical divergence angle of synchrotron radiation is given approximately by $m_0 c_2/E$, where m_0 is the electron rest mass, c is the velocity of light and E is the electron energy. This value is typically 10^{-4} rad. The topographic resolution (R_x) is decided by the source size in the incidence plane (S_x), source-specimen distance (D) and the specimen-film distance (d) and it can be given by[2]

$$R_x = dS_x/D$$

The theoretical resolution so obtained is ~0.4 µm for Beamline X19C at National Synchrotron Light Source and ~0.06 µm for Beamline XOR-33BM /UNI-CAT at Advanced Photon Source if D=10 cm is used (vertical reflection geometry).

1.2 Contrast Mechanism of X-ray Diffraction Topography

Contrast, which means the point to point variation in diffracted intensity, is generally understood in terms of two mechanisms: orientation contrast and extinction contrast. Basically the topographic contrast arises due to changes in the of x-ray wave-fields in the crystals and may or may not be associated with strain in the crystals. Orientation contrast arises when parts of the sample are oriented such that they do not satisfy the Bragg condition. Thus there is an undarkened patch on the film. To understand orientation contrast, one can imagine a monochromatic X-ray beam incident on a sample composed of areas that are crystallographically misoriented compared to the rest of the crystal. If these areas are misoriented sufficiently such that they are outside the reflection range of the crystal, they

cannot satisfy the Bragg condition and therefore they will not diffract. For areas that are less misoriented, the diffracted intensity can take on any value from negligible to nearly the intensity diffracted by the surrounding crystal. Schematic of orientation contrast form monochromatic x-ray is shown in Fig.2. Orientation contrast usually associates with twins, sub-grains and where sudden orientation change happens. Under the low absorption conditions used in our study, orientation contrast dominates contrast contributions to the image. Ray tracing simulation work is based on this mechanism. Another type of orientation contrast arises when continuous radiation is being used. It is common in synchrotron radiation. Simple images occur where the crystal contains discrete mosaic blocks, but when the lattice distortion is continuous, the resulting contrast can be very complex and difficult to interpret.
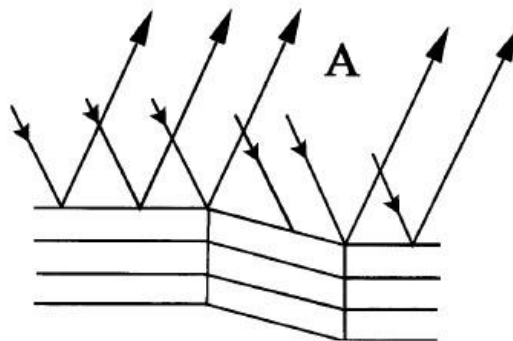
Figure 2: Schematic of orientation contrast from monochromatic x-ray

Extinction contrast is described by means of dynamical and kinematical x-ray diffraction theories. The distortion of the lattice around a defect gives rise to a different scattering power from that of the surrounding matrix. In all cases, it arises from a breakdown or change of the dynamical diffraction in the perfect crystal. In classical structure analysis, the name extinction was used to describe the observation that the integrated intensity was less than that predicted by the kinematical theory. Around the defect, enhanced scattering was observed and this 'loss of extinction' is the origin of the name. In this study, dislocations appear as white lines or dots in grazing topographic images.

1.3 Penetration Depth

The concept of penetration depth is very important in this study. It gives information about the crystal volume imaged and thus helps in the understanding of the defect configurations. In stress mapping, the relationship between stress and depth is built based on penetration depth. Penetration depth is defined as the depth (t) at which intensity drops to 1/e.
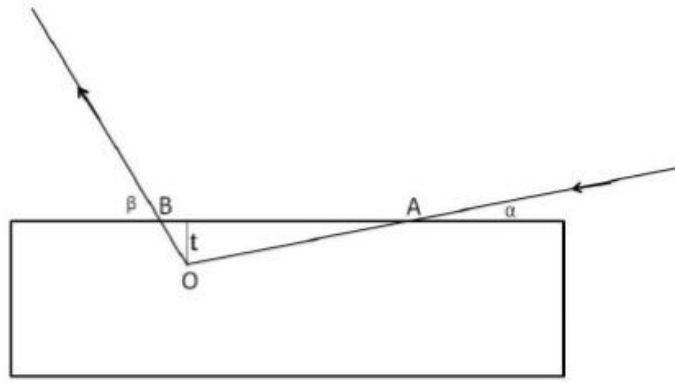
Figure 3: Schematic of penetration depth

As shown in Fig. 3, AO is incident beam, OB is exit beam, plane AB is the surface of crystal and t is penetration depth. From the picture, the value of AO and BO could be written as,

$$AO = \frac{t}{\sin a}, \quad OB = \frac{t}{\sin \beta}$$

Total path lengths that x-ray go through the crystal:

$$\tau = OA + OB = \frac{t}{\sin a} + \frac{t}{\sin \beta}$$

By the definition of absorption effect of x-ray

$$\frac{I}{I_0} = e^{-\mu\tau}$$

By the definition of penetration depth

$$e^{-\mu\tau} = \frac{1}{e}$$

Therefore,

$$\mu\tau = 1,$$

$$\mu\left(\frac{t}{\sin a} + \frac{t}{\sin \beta}\right) = 1$$

$$t = \frac{1}{\mu(\frac{1}{\sin \alpha} + \frac{1}{\sin \beta})}$$

where μ is the absorption coefficient, α is the incident angel, β is the exit angel.

This equation, which is based on photoelectric absorption, could be used for ordinary penetration depth calculation. For nearly defect free crystal, penetration depth is governed by extinction distance. Penetration depth z_e in this situation is given by,

$$z_e = \frac{\Lambda}{2\pi\sqrt{1 - \eta^2}},$$

where Λ is the extinction distance, η is deviation parameter (the deviation from the rocking

curve peak).

1.4 Proof of $\vec{n} = \vec{n_0} - \nabla(\vec{n_0} \cdot \vec{u})$

As mentioned above, it is the topography of crystal lattice planes that are examined. Therefore, if the crystal plane is distorted by stress, the plane normal after distortion $\vec{n}$ could be calculated using the equation $\vec{n} = \vec{n_0} - \nabla(\vec{n_0} \cdot \vec{u})$, where $\vec{n_0}$ is the plane normal before distortion and $\vec{u}$ is the stress field that applied onto the plane. This equation acts as the fundamental of two techniques associated with XRT: stress mapping via x-ray topography (SMART) and ray tracing simulation. The equation could be proved as the following[3].

Consider a crystallographic plane occupy the coordination as shown in Fig.4:
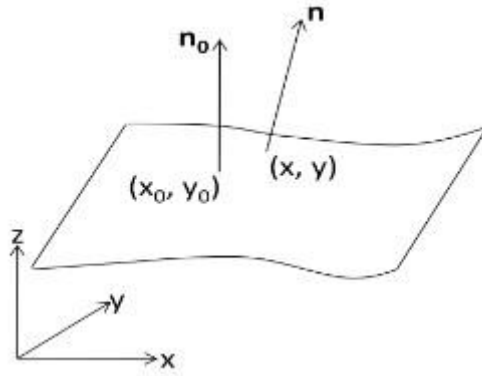
Figure 4: Schematic of the crystal plane normal before and after distortion at an arbitrary position[3]

Assume the equation of the surface as

$z=f(x, y)$ Equation 1.4.1

or, $F(x, y, z)=f(x, y)-z=0$ Equation 1.4.2

Plane normal vector at any general location can be written as:

$\vec{n}(x,y,z) = \nabla[\vec{F}(x,y,z)]$ Equation 1.4.3

Applying Taylor's expansion to function f, we can get

$f(x,y) = f(x_0, y_0) + (\frac{\partial f(x_0, y_0)}{\partial x}(x - x_0) + \frac{\partial f(x_0, y_0)}{\partial y}(y - y_0))$ Equation 1.4.4

The displacement could be written as

$$\vec{r} = (x - x_0)\vec{i} + (y - y_0)\vec{j} \qquad \text{Equation 1.4.5}$$

Now, consider the term of $\vec{r} \cdot \nabla[f(x_0, y_0) - z]$,

$$\vec{r} \cdot \nabla[f(x_0, y_0) - z] = [(x - x_0)\vec{i} + (y - y_0)\vec{j}]\left[\frac{\partial f(x_0, y_0)}{\partial x}\vec{i} + \frac{\partial f(x_0, y_0)}{\partial y}\vec{j} - k\right]$$

$$= \frac{\partial f(x_0, y_0)}{\partial x}(x - x_0) + \frac{\partial f(x_0, y_0)}{\partial y}(y - y_0)$$

Substitute the result into Equation 1.4.4, we have

$$f(x, y) = f(x_0, y_0) + \vec{r} \cdot \nabla[f(x_0, y_0) - z] \qquad \text{Equation 1.4.6}$$

or, $f(x, y) - z = f(x_0, y_0) - z + \vec{r} \cdot \nabla[f(x_0, y_0) - z]$

or, $\nabla[f(x, y) - z] = \nabla[f(x_0, y_0) - z] + \nabla[\vec{r} \cdot \nabla[f(x_0, y_0) - z]]$

or, $\vec{n} = \overrightarrow{n_0} - \nabla(\overrightarrow{n_0} \cdot \vec{r})$ \qquad Equation 1.4.7

$\vec{r}$ is the displacement in the equation which has the same meaning with $\vec{u}$.

This equation gives us a straightforward way to calculate the plane normal after the distortion associated with the dislocation, by knowing the displacement field of the dislocation. The displacement fields for different dislocations will be shown in the next chapter.

1.5 Solid Mechanics

To better understand the mechanism of stress mapping in this study, basic solid mechanic background knowledge will be introduced here. Stress is defined as the average force per unit area that some particle of a body exerts on an adjacent particle, across an imaginary surface that separates them. According to Hooke's law, the relationship between stress and strain can be written in contracted notation as

$$\sigma_{ij} = C_{ijkl}\varepsilon_{kl} \qquad i, j = 1, 2, \dots, 6 \qquad \text{Equation 1.5.1}$$

where σ_i are the stress components shown in Fig. 5, C_{ij} is the stiffness matrix, and ε_j are the strain components.
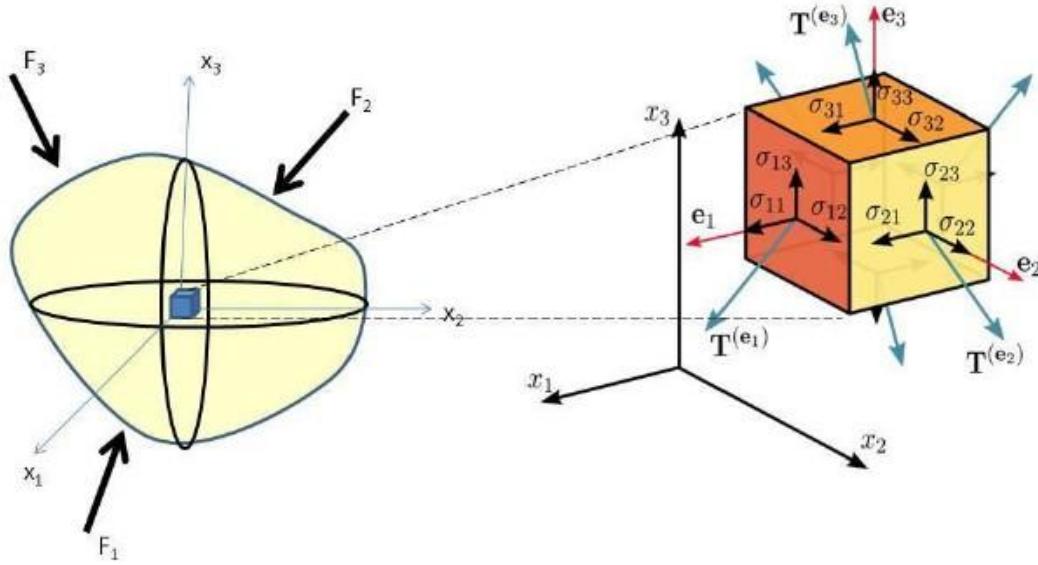
Figure 5: Stress on an Element[4]

In general, stress tensor has nine components where i and j can have value 1, 2 or 3. It can be shown that $\sigma_{ij} = \sigma_{ji}$, therefore total number of independent stress components reduces to six. It could be written as:

$$\sigma_{ij} = \begin{bmatrix} \sigma_{11} & \sigma_{12} & \sigma_{13} \\ \sigma_{21} & \sigma_{22} & \sigma_{23} \\ \sigma_{31} & \sigma_{32} & \sigma_{33} \end{bmatrix}$$

where $\sigma_{12} = \sigma_{21}$, $\sigma_{13} = \sigma_{31}$, $\sigma_{31} = \sigma_{32}$.

As for stain, it is defined as a normalized measure of deformation representing the displacement between particles in the body relative to a reference length. It is a tensor as

$$\varepsilon_{ij} = \frac{1}{2}\left(\frac{\partial u_i}{\partial j} + \frac{\partial u_j}{\partial i}\right) = \begin{bmatrix} \varepsilon_{xx} & \varepsilon_{xy} & \varepsilon_{xz} \\ \varepsilon_{yx} & \varepsilon_{yy} & \varepsilon_{yz} \\ \varepsilon_{zx} & \varepsilon_{zy} & \varepsilon_{zz} \end{bmatrix} = \begin{bmatrix} \frac{\partial u_x}{\partial x} & \frac{1}{2}\left(\frac{\partial u_x}{\partial y} + \frac{\partial u_y}{\partial x}\right) & \frac{1}{2}\left(\frac{\partial u_x}{\partial z} + \frac{\partial u_z}{\partial x}\right) \\ \frac{1}{2}\left(\frac{\partial u_x}{\partial y} + \frac{\partial u_y}{\partial x}\right) & \frac{\partial u_y}{\partial y} & \frac{1}{2}\left(\frac{\partial u_y}{\partial z} + \frac{\partial u_z}{\partial y}\right) \\ \frac{1}{2}\left(\frac{\partial u_x}{\partial z} + \frac{\partial u_z}{\partial x}\right) & \frac{1}{2}\left(\frac{\partial u_y}{\partial z} + \frac{\partial u_z}{\partial y}\right) & \frac{\partial u_z}{\partial z} \end{bmatrix},$$

where *u* is the displacement.

In general, there are a total of $3^4 = 81$ constants in stiffness matrix, but there is relation between the components which leads to fewer numbers of elastic constants. It has been proved that $\varepsilon_{kl} = \varepsilon_{lk}$ and $C_{ijkl} = C_{jikl}$. With the foregoing reduction from 36 to 21 independent constants, the stress-strain relations are

$$\begin{bmatrix} \sigma_1 \\ \sigma_2 \\ \sigma_3 \\ \sigma_4 = \sigma_{23} \\ \sigma_5 = \sigma_{31} \\ \sigma_6 = \sigma_{12} \end{bmatrix} = \begin{bmatrix} C_{11} & C_{12} & C_{13} & C_{14} & C_{15} & C_{16} \\ C_{12} & C_{22} & C_{23} & C_{24} & C_{25} & C_{26} \\ C_{13} & C_{23} & C_{33} & C_{34} & C_{35} & C_{36} \\ C_{14} & C_{24} & C_{34} & C_{44} & C_{45} & C_{46} \\ C_{15} & C_{25} & C_{35} & C_{45} & C_{55} & C_{65} \\ C_{16} & C_{26} & C_{36} & C_{46} & C_{56} & C_{66} \end{bmatrix} \begin{bmatrix} \varepsilon_1 \\ \varepsilon_2 \\ \varepsilon_3 \\ \gamma_{23} = 2\varepsilon_{23} \\ \gamma_{31} = 2\varepsilon_{31} \\ \gamma_{12} = 2\varepsilon_{12} \end{bmatrix}.$$

Expand this matrix:

$$\sigma_1 = C_{11}\varepsilon_1 + C_{12}\varepsilon_2 + C_{13}\varepsilon_3 + 2C_{14}\varepsilon_{23} + 2C_{15}\varepsilon_{31} + 2C_{16}\varepsilon_{12}$$
$$\sigma_2 = C_{12}\varepsilon_1 + C_{22}\varepsilon_2 + C_{23}\varepsilon_3 + 2C_{24}\varepsilon_{23} + 2C_{25}\varepsilon_{31} + 2C_{26}\varepsilon_{12}$$
$$\sigma_3 = C_{13}\varepsilon_1 + C_{23}\varepsilon_2 + C_{33}\varepsilon_3 + 2C_{34}\varepsilon_{23} + 2C_{35}\varepsilon_{31} + 2C_{36}\varepsilon_{12}$$
$$\sigma_4 = C_{14}\varepsilon_1 + C_{24}\varepsilon_2 + C_{34}\varepsilon_3 + 2C_{44}\varepsilon_{23} + 2C_{45}\varepsilon_{31} + 2C_{46}\varepsilon_{12}$$
$$\sigma_5 = C_{15}\varepsilon_1 + C_{25}\varepsilon_2 + C_{35}\varepsilon_3 + 2C_{45}\varepsilon_{23} + 2C_{55}\varepsilon_{31} + 2C_{65}\varepsilon_{12}$$
$$\sigma_6 = C_{16}\varepsilon_1 + C_{26}\varepsilon_2 + C_{36}\varepsilon_3 + 2C_{46}\varepsilon_{23} + 2C_{56}\varepsilon_{31} + 2C_{66}\varepsilon_{12}$$

This is the most general expression within the framework of linear elasticity, which means, in a general crystal, having least crystallographic symmetry elements with arbitrary orientation, total number of independent elastic constant is 21. Actually, the relations in above matrix are referred to as characterizing anisotropic material for there are no planes of symmetry for the material properties. As the symmetry elements in the crystal increases, the total number of independent elastic constants decreases. If there is one plane of material property symmetry, such material is termed as monoclinic and has 13 independent elastic constants. If there are two orthogonal planes of material property symmetry for a material, symmetry will exist relative to a third mutually orthogonal plane and only 9 independent constants in the stiffness matrix. If at every point of material there is one plane in which the mechanical properties are equal in all directions, 5 independent constants exist in this so-called transversely isotropic material.

As for isotropic material which is defined as a material where exist an infinite number of planes of property symmetry, the foregoing relations get simplified with only 2 independent constants in the stiffness matrix:

$$\begin{bmatrix} \sigma_1 \\ \sigma_2 \\ \sigma_3 \\ \sigma_4 = \sigma_{23} \\ \sigma_5 = \sigma_{31} \\ \sigma_6 = \sigma_{12} \end{bmatrix} = \begin{bmatrix} C_{11} & C_{12} & C_{12} & 0 & 0 & 0 \\ C_{12} & C_{11} & C_{12} & 0 & 0 & 0 \\ C_{12} & C_{12} & C_{11} & 0 & 0 & 0 \\ 0 & 0 & 0 & (C_{11}-C_{12})/2 & 0 & 0 \\ 0 & 0 & 0 & 0 & (C_{11}-C_{12})/2 & 0 \\ 0 & 0 & 0 & 0 & 0 & (C_{11}-C_{12})/2 \end{bmatrix} \begin{bmatrix} \varepsilon_1 \\ \varepsilon_2 \\ \varepsilon_3 \\ \gamma_{23} = 2\varepsilon_{23} \\ \gamma_{31} = 2\varepsilon_{31} \\ \gamma_{12} = 2\varepsilon_{12} \end{bmatrix}.$$

As we know, the value of C_{11}, C_{12} and some other elastic constants are set in some certain crystalline direction in the sample, and the coordination system inside the crystal is not always the same as the actual coordination system. Therefore, the process of tensor transformation has to be conducted here. Elastic constants could be transformed to new axes by applying standard tensor transformation equation:

$$C'_{ijkl} = a_{im}a_{jn}a_{ko}a_{lp}C_{mnop}$$

where a_{ij} is the cosine value of the angel between x-axis and x'-axis.

In the calculation process, the relationship between two coordinate systems could be written as:

$$\begin{bmatrix} x' \\ y' \\ z' \end{bmatrix} = \begin{bmatrix} \cos x'x & \cos x'y & \cos x'z \\ \cos y'x & \cos y'y & \cos y'z \\ \cos z'x & \cos z'y & \cos z'z \end{bmatrix} \cdot \begin{bmatrix} x \\ y \\ z \end{bmatrix}$$

If the rotation angle of each axis is determined, the relationship could be written as:

$$\begin{bmatrix} x' \\ y' \\ z' \end{bmatrix} = \begin{bmatrix} \cos c & -\sin c & 0 \\ \sin c & \cos c & 0 \\ 0 & 0 & 1 \end{bmatrix} \cdot \begin{bmatrix} \cos b & 0 & \sin b \\ 0 & 1 & 0 \\ -\sin b & 0 & \cos b \end{bmatrix} \cdot \begin{bmatrix} 1 & 0 & 0 \\ 0 & \cos a & \sin a \\ 0 & -\sin a & \cos a \end{bmatrix} \cdot \begin{bmatrix} x \\ y \\ z \end{bmatrix}$$

where c, b and a are rotation angle of z-axis, y-axis and x-axis.

In this study, silicon sample is tested. Elastic constants of silicon are:

$C_{11} = 165.7, C_{22} = 63.9, C_{33} = 79.6\text{Gpa}$

These constants represent when the crystal is oriented such that crystallographic direction [100], [010] and [001]. But in this study, the coordinate system in the experiment is not the same as the one inside crystal. Therefore, elastic constants here could be calculated using the following codes:

```
A={{1/Sqrt[2],0,-1/Sqrt[2]},{-(1/Sqrt[2]),0,-(1/Sqrt[2])},{0,1,0}};
stiffness=Table[0,{i,1,3},{j,1,3},{k,1,3},{l,1,3}];
stiffness[[1]][[1]][[1]][[1]]=stiffness[[2]][[2]][[2]][[2]]=stiffness[[3]][[3]][[3]][[3]]=165.7;
stiffness[[1]][[1]][[2]][[2]]=stiffness[[2]][[2]][[3]][[3]]=stiffness[[3]][[3]][[1]][[1]]=stiffness[[2]][[2]][[1]][[1]]=stiffness[[3]][[3]][[2]][[2]]=stiffness[[1]][[1]][[3]][[3]]=63.9;
stiffness[[3]][[2]][[3]][[2]]=stiffness[[3]][[2]][[2]][[3]]=stiffness[[2]][[3]][[3]][[2]]=stiffness[[2]][[3]][[2]][[3]]=stiffness[[3]][[1]][[3]][[1]]=stiffness[[3]][[1]][[1]][[3]]=stiffness[[1]][[3]][[3]][[1]]=stiffness[[1]][[3]][[1]][[3]]=stiffness[[2]][[1]][[2]][[1]]=stiffness[[2]][[1]][[1]][[2]]=stiffness[[1]][[2]][[2]][[1]]=stiffness[[1]][[2]][[1]][[2]]=79.6;
Cstiff=Table[Sum[A[[m]][[i]] A[[n]][[j]] A[[o]][[k]] A[[p]][[l]]
stiffness[[i]][[j]][[k]][[l]],{i,1,3},{j,1,3},{k,1,3},{l,1,3}],{m,1,3},{n,1,3},{o,1,3},{p,1,3}];
c11=Cstiff[[1,1,1,1]];c22=Cstiff[[2,2,2,2]];
c33=Cstiff[[3,3,3,3]];c44=Cstiff[[2,3,2,3]];
c55=Cstiff[[1,3,1,3]];c66=Cstiff[[2,1,2,1]];
c12=Cstiff[[1,1,2,2]];c13=Cstiff[[1,1,3,3]];
c23=Cstiff[[2,2,3,3]];
```

Chapter II. Characterization of Threading Dislocation in Hydrothermal Grown ZnO Substrates

2.1 Introduction of ZnO

Zinc oxide is a promising semiconductor of the II-VI semiconductor group with many desirable properties, including good transparency, strong room temperature luminescence, high electron mobility, wide band gap (3.37ev) and large extinction energy (60mev) at room temperature[5,6], which could make it highly suitable for transparent electrodes in-liquid crystal displays, energy-saving or heat-protecting windows, electronics as thin-film transistors, light-emitting diodes and as a substrate material for GaN-based devices. ZnO single crystal substrate is also perfect for homo-epitaxy of ZnO active layers for its perfect lattice matching and relative low dislocation density.
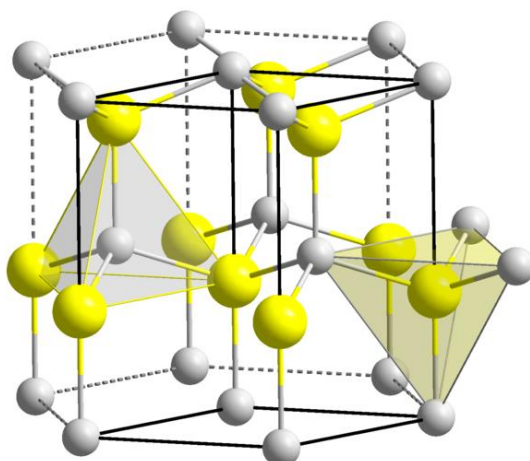
Figure 6: Schematic of wurtzite structure[7]

Actually, there are two main crystalline structures for zinc oxide: wurtzite and zincblende. The former one is most common for it is stable at ambient conditions. The samples we have in this study adopt the wurtzite structure. Wurtzite structure, as shown in Fig. 6, could be view as two hexagonal structures interpenetrating into each other. It has a point group 6 mm, and the space group is $P6_3mc$. The lattice parameters are a= 3.252 Å, c = 5.313 Å and the c/a ration is close to the ideal value for hexagonal structure (1.633). The atom position in the crystal lattice is shown in table 1 and some properties of zinc oxide are listed in table 2.

	Atom	X	Y	Z	Occupancy
1	Zn	0	0	0	1
2	Zn	0.3333	0.6667	0.5	1
3	O	0	0	0.375	1
4	O	0.3333	0.6667	0.875	1

Table 1: Atom positions in the crystal

Molar Mass	Density	Melting Point	Boiling Point	Solubility in Water	ΔH^{θ}_{298}	S^{θ}_{298}
81.408g/mol	5.606g/cm^3	1975°C	1975°C	0.16mg/100ml(30°C)	-348kJ/mol	43.9JK^{-1}mol^{-1}

Table 2: Some properties of zinc oxide

Generally speaking, the most closely packed crystallographic planes are slip planes in most crystals. In wurtzite structure, (0001) planes are the most closely packed planes. Thus, the first type prismatic planes are of the form $\{10\bar{1}0\}$, while the second type prismatic planes are of the form $\{\bar{1}2\bar{1}0\}$. From the dislocation theory, we have:

$$\text{E(screw)} = \frac{Gb^2}{4\pi}\ln\frac{R}{r_0} \qquad\qquad \text{Equation 2.1.1}$$

$$\text{E(edge)} = \frac{Gb^2}{4\pi(1-\vartheta)}\ln\frac{R}{r_0} \qquad\qquad \text{Equation 2.1.2}$$

where R is the outer radius, r_0 is the center radius, ϑ is poisson's ration and b is the burger's vector.

From the equations above, the elastic energy of dislocation is proportional to b^2, the shortest lattice translation vectors are Burger's vectors of lowest energy dislocations. Therefore, the slip directions in wurtzite are $1/3[11\bar{2}0]$ and [0001]. The slip system in wurtzite is a little complex. Energetically, most preferred slip system is (0001) with $<11\bar{2}0>$. Other slip systems are also found in wurtzite structure, such as (0001) with $<10\bar{1}0>$, $\{10\bar{1}0\}$ with $<11\bar{2}0>$, $\{10\bar{1}0\}$ with [0001] and $\{\bar{1}2\bar{1}0\}$ with $<10\bar{1}0>$.

The wurtzite structure consists of triangularly arranged alternating bi-atomic close-packed (0001) planes, for example, Zn and O pairs, thus the stacking sequence of the (0001) plane is *AaBbAaBb*… in the [0001] direction, which is usually the growth direction.

2.2 Hydrothermal Method

Hydrothermal growth is defined as a method of synthesis of single crystals that depends on the solubility of minerals in hot water under high pressure. The crystal growth is performed in an apparatus consisting of a steel pressure vessel called autoclave, in which a nutrient is supplied along with water. A gradient of temperature is maintained at the opposite ends of the growth chamber so that the hotter end dissolves the nutrient and the cooler end causes seeds to take additional growth. Note that the sample in this study is grown by Tokyo Denpa.

In 1905, Spezia got success in synthetizing quartz crystals, and it marked that the technique of hydrothermal synthesis has come into truth. The epoch-making achievement spent him about six months and finally, the man-made crystal could be found to grow on the crystal seed. But at that time, not enough fundamental knowledge has been built thus scientists could not fully understand the mechanism of hydrothermal synthesis. During World War II, a great shortage of piezoelectric quartz, which is a kind of strategic supply material, stimulate a large amount of investments into hydrothermal synthesis. Therefore, the technique got development after that. In recent years, Nathan Jonann Nicholas[8] has found the mechanism for hydrothermal growth of zinc oxide and they proved that in hydrothermal process, the final zinc oxide crystal adopts the wurtzite structure.

Typical Conditions
T_1 : 345° C
T_2 : 355° C
Pressure : 1-2 kbars
Fill - 70-85% Vol.
Solvent LiOH/KOH
Duration : 20-50 days

T_1

T_2

Lower %
ZnO Solubility

Higher %
ZnO Solubility
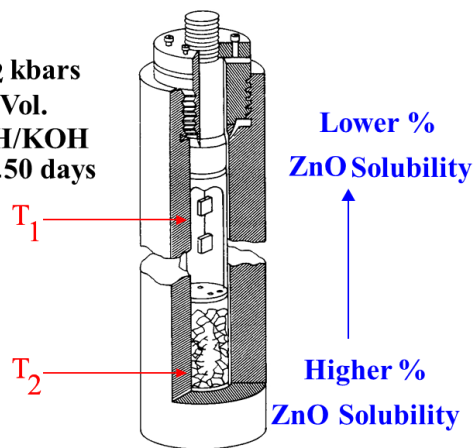
Figure 7: Schematic of hydrothermal method in this study

There are some features for hydrothermal method: (1) the process is performed in an in-closed system with adjustable temperature and pressure; (2) temperature here is relatively lower than molten salt growth; (3) temperature gradient is quite small in the growth area; (4) the solution has a low viscosity.

Possible advantages of the hydrothermal method over other types of crystal growth include the ability to create crystalline phases which are not stable at the melting point. Also,

materials which have a high vapor pressure near their melting points can also be grown by the hydrothermal method. The method is also particularly suitable for the growth of large good-quality crystals while maintaining good control over their composition. Disadvantages of the method include the need of expensive autoclaves, and the impossibility of observing the crystal as it grows.

2.3 Fundamentals Aspects of Dislocation Theory

There are various dislocations in zinc oxide single crystal, including edge dislocations, screw dislocations, mixed dislocations, basal plane dislocations. Threading dislocations are those propagate throughout the crystal in growth direction or with some tilts, which is <0001>. Actually, stacking faults are not observed in this sample. In general, there are mainly three types of threading dislocations: threading edge dislocation (TED), threading screw dislocation (TSD) and $c+a$ (mixed) dislocation. Threading screw dislocations are growth dislocations in screw orientation with line direction along [0001] and Burger's vector n<0001> (n is an integer); if n is greater or equal to 2, the dislocations are called Micro-pipe; they are considered to be empty core screw dislocations with larger strain energy. TEDs are dislocations with line direction roughly parallel to c-axis and Burger's vector in c-plane. Mixed dislocations have features of both TEDs and TSDs. Its Burger's vector equals the vector sum of its edge component and screw component. Basal plane dislocations (BPD) are glissile dislocations with both line direction and Burger's vector in c-plane. The presence of these defects will strongly influence the performance, lifetime, reliability of the devices that grown on these substrates. Threading dislocations, which will propagate into devices, have much more damage to the devices; while BPDs, which mainly lie on the basal plane beneath the surface, do not intend to perform negative influences. Thus it is of great importance to conduct detailed characterization on the threading dislocations in zinc oxide. An overview of threading dislocations is shown in the following table.

	Line Direction	Burger's vector
TED	Roughly parallel to growth direction[0001]	1/3<11-20>(3.426Å)
TSD	Roughly parallel to growth direction[0001]	n<0001>(5.313nÅ)
MPs	Parallel to growth direction[0001]	n<0001>
c+a	Roughly parallel to growth direction[0001]	1/3<11-20>+n<0001>

n is an integer

Table 3. Details of Threading Dislocations

To fully understand the mechanism of XRT and the contrast in simulated images, the displacement of each type of threading dislocations will be discussed here. Furthermore, in order to release stress on the free surface for threading screw dislocations, surface relaxation effect will be introduced latter.
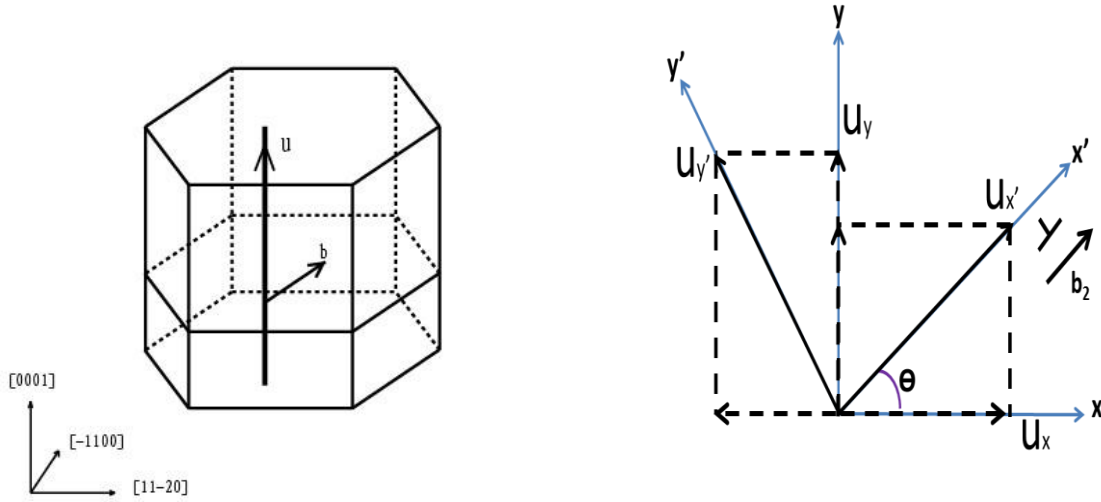
Figure 8: (a) schematic of *u* and *b* in TED (general case)   (b) displacement transformation

The relationship between TED's dislocation line direction and Burger's vector is shown in Fig.8 (a). According to dislocation theory, the stress field of threading edge dislocation is[9]:

$$u_x = \frac{b_1}{2\pi}\left[\tan^{-1}\frac{y}{x} + \frac{xy}{2(1-v)(x^2+y^2)}\right],$$ Equation 2.3.1

$$u_y = -\frac{b_1}{2\pi}\left[\frac{1-2v}{4(1-v)}\ln(x^2+y^2) + \frac{x^2-y^2}{4(1-v)(x^2+y^2)}\right],$$ Equation 2.3.2

where v is the Poisson's ration of ZnO (0.351 without porosity); b_1 is Burger's vector of TED.

In this study, x-axis here is set to have the same direction with [11-20]; the term u_x means the displacement in [11-20]. Actually, in general conditions, the x-axis is not always parallel to the direction of [11-20]; therefore, a coordinate with u_x' and u_y' is built, which is going to be used in simulating the TED images in grazing incidence geometry. It is set parallel to the projection of the reflection vector on the basal plane. The transformation is as follows:

$$u_x' = u_x\cos\theta - u_y\sin\theta\,;$$ Equation 2.3.3
$$u_y' = u_x\sin\theta + u_y\cos\theta$$ Equation 2.3.4
where θ is the angle between two coordinates.
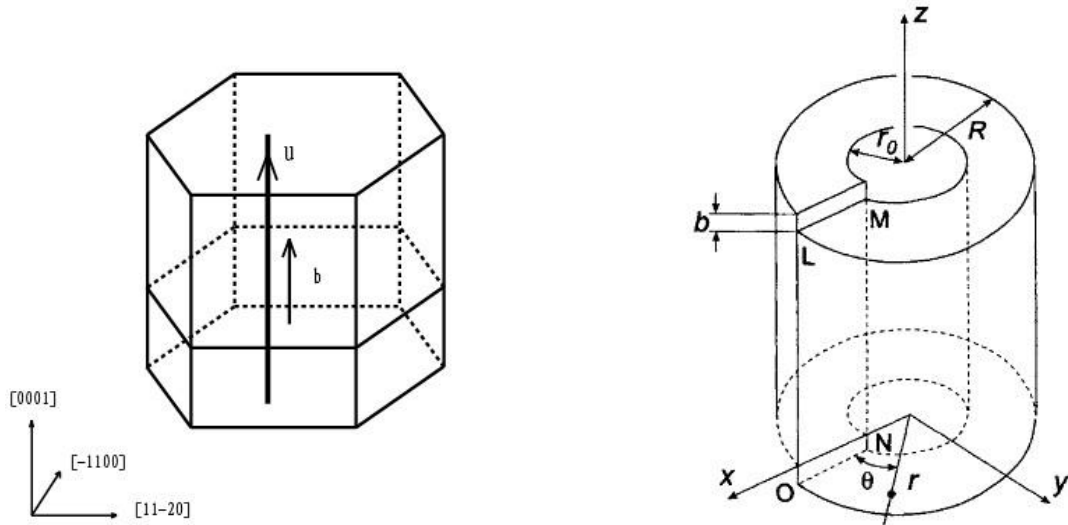
Figure 9:(a) schematic of threading screw dislocation (b) distortion produced by screw dislocation

Situation for threading screw dislocations and MPs is much more complicated. TSDs and MPs are screw dislocations with different magnitude. They are shown in Fig. 9. According to basic dislocation theory, the displacement only has c-component[10]:

$$u_z = \frac{b_2}{2\pi} \tan^{-1} \frac{y}{x},$$ Equation 2.3.5

$$u_x = u_y = 0;$$ Equation 2.3.6

where b_2 is the Burger's vector of threading screw dislocations.

When TSDs are close to the surface, the strain component perpendicular to the crystal surface has to be zero in order to satisfy the free surface condition. An additional in-plane (*c*-plane) displacement is thus resulted due to such surface relaxation effect, which was deduced by Yoffe[11]. To illustrate surface relaxation effect, a semi-infinite surface model is introduced here.
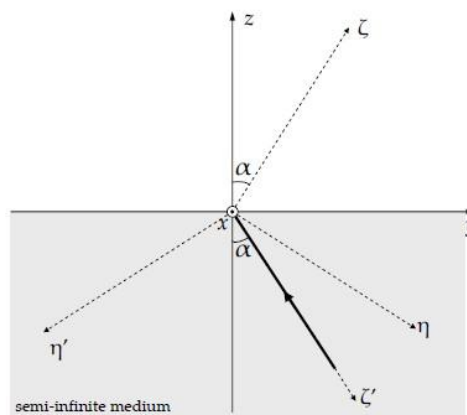
Figure 10: Semi-infinite surface model

Assume there is a dislocation locates near the surface area with Burger's vector b, which could be divided into b_x, b_y and b_z. Therefore, the displacement associated with b_x component could be written as,

$$2\mu u_x = z\frac{\partial^2\varphi}{\partial x\partial z} + (1-2v)\frac{\partial\varphi}{\partial x} \ ,$$

$$2\mu u_y = z\frac{\partial^2\varphi}{\partial y\partial z} + (1-2v)\frac{\partial\varphi}{\partial y} \ ,$$

$$2\mu u_x = z\frac{\partial^2\varphi}{\partial^2 z} + 2(1-v)\frac{\partial\varphi}{\partial z} \ ,$$

where

$$\varphi = \frac{\mu b_x \cot a}{2\pi(1-v)}\Big\{\zeta\log(r-\zeta) + 2(1-v)r + (1-2v)z\log(r-z) + 2(1-v)\cot a\Big[\eta\log(r-$$

$$\zeta) - y\log(r-z) - x\Big(\tan^{-1}\frac{y}{x} - \tan^{-1}\frac{\eta}{x} + \tan^{-1}\frac{xr\sin a}{x^2\cos a + y\eta}\Big)\Big]\Big\},$$

$\mathrm{r} = \sqrt[2]{x^2 + y^2 + z^2}$,

$\eta = y\cos a - z\sin a,$
$\zeta = y\sin a + z\cos a,$
$\eta' = -y\cos a - z\sin a,$
$\zeta' = y\sin a - z\cos a.$

The displacement field associated with the Burgers vector component b_y is:

$$2uu_x = \frac{ub_y}{4\pi(1-v)}\cos a\Big[-\frac{x^2}{r(r-\zeta)} - \frac{x^2}{r(r-\zeta)} + (1-2v)\log(r-\zeta)(r-\zeta')\Big] + z\frac{\partial^2\varphi}{\partial x\partial z}$$

$$+ (1-2v)\frac{\partial\varphi}{\partial x},$$

$$2uu_y = \frac{\mu b_y}{4\pi}\Big(\tan^{-1}\frac{\eta}{x} - \tan^{-1}\frac{\eta'}{x} + \tan^{-1}\frac{xr\sin 2a}{\eta\eta' - x^2\cos 2a}\Big)$$

$$+ \frac{\mu b_y}{4\pi(1-v)}\Big[\frac{\sin a\cos a}{r-\zeta} + \frac{\sin a\cos a}{r-\zeta'} - \frac{y\cos a}{r(r-\zeta)} - \frac{y\cos a}{r(r-\zeta')}\Big] + z\frac{\partial^2\varphi}{\partial y\partial z}$$

$$+ (1-2v)\frac{\partial\varphi}{\partial y},$$

$$2uu_z = \frac{\mu b_y}{4\pi(1-v)}\Big[\frac{\cos^2 a}{r-\zeta} + \frac{\cos^2 a}{r-\zeta'} - \frac{z\cos a}{r(r-\zeta)} - \frac{z\cos a}{r(r-\zeta')}\Big] + z\frac{\partial^2\varphi}{\partial z^2} - 2(1-v)\frac{\partial\varphi}{\partial z},$$

where $\varphi = \frac{vub_y}{2\pi(1-v)}\Big[\frac{xz}{r-z}x\log(r-z)\Big]$,

The displacement field associated with the Burgers vector component bz is:

$$2uu_x = \frac{ub_z \sin a}{4\pi(1-v)}\left[(1-2v)\log(r-\zeta)(r-\zeta') - \frac{x^2}{r(r-\zeta)} - \frac{x^2}{r(r-\zeta')}\right] + \frac{ub_z y}{\pi(r-z)}$$

$$+ z\frac{\partial^2\varphi}{\partial x \partial z} + (1-2v)\frac{\partial\varphi}{\partial x},$$

$$2uu_y = \frac{ub_z x \sin a}{4\pi(1-v)}\left[\frac{\sin a}{r-\zeta} + \frac{\sin a}{r-\zeta'} - \frac{y}{r(r-\zeta)} - \frac{y}{r(r-\zeta')}\right] - \frac{ub_z x}{\pi(r-z)} + z\frac{\partial^2\varphi}{\partial y \partial z}$$

$$+ (1-2v)\frac{\partial\varphi}{\partial y},$$

$$2uu_z = \frac{ub_z}{2\pi}\left(\tan^{-1}\frac{\eta}{x} - \tan^{-1}\frac{\eta'}{x} + \tan^{-1}\frac{xr \sin 2a}{\eta\eta' - x^2 \cos 2a}\right)$$

$$+ \frac{ub_z x \sin a}{4\pi(1-v)}\left[\frac{\cos a}{r-\zeta} + \frac{\cos a}{r-\zeta'} - \frac{z}{r(r-\zeta)} - \frac{z}{r(r-\zeta')}\right] + z\frac{\partial^2\varphi}{\partial z^2}$$

$$- 2(1-v)\frac{\partial\varphi}{\partial z},$$

where

$$\varphi = \frac{ub_z}{2\pi(1-v)}\left[-x \sin a \log(r-\zeta) + z\left(\tan^{-1}\frac{y}{x} - \tan^{-1}\frac{\eta}{x} + \tan^{-1}\frac{xr \sin a}{x^2 \cos a + y\eta}\right)\right].$$

Displacement fields resulted from surface relaxation effect could be calculated in simulation work using the above equations. In this study, the infinite plate/disc type surface relaxation obtained by Eshelby and Stroh[12] is used. Therefore, stress field in TSDs and MPs is given by,

$$u_x = u_\theta \frac{-y}{\sqrt{x^2 + y^2}}, \qquad\qquad\qquad\qquad\qquad \text{Equation 2.3.7}$$

$$u_y = u_\theta \frac{x}{\sqrt{x^2 + y^2}}, \qquad\qquad\qquad\qquad\qquad \text{Equation 2.3.8}$$

$$u_z = \frac{b_2}{2\pi}\tan^{-1}\frac{y}{x}. \qquad\qquad\qquad\qquad\qquad \text{Equation 2.3.9}$$

$$u_\theta = \frac{-b_2}{2\pi}\sum_{n=0}^{\infty}(-1)^n\left\{\frac{\sqrt{x^2 + y^2}}{(2n+1)t - (z+t) + \sqrt{[(2n+1)t - z]^2 + (x^2 + y^2)}}\right.$$

$$\left. - \frac{\sqrt{x^2 + y^2}}{(2n+1)t + (z+t) + \sqrt{[(2n+1)t + z]^2 + (x^2 + y^2)}}\right\} \quad \text{Equation 2.3.10}$$

where t is the half thickness of the sample, b_2 is Burger's vector of threading screw dislocation.

As for c+a dislocation, its stress field could be considered that the stress field is the sum of a-component and c-component[9]. Burger's vector has to be carefully calculated for c+a

dislocations.

2.4 Simulation Process

Ray tracing simulation work is extremely useful in characterization of threading dislocations when not enough reflections are accessible. As mentioned before, threading dislocations are dislocations that could run through the crystal in growth direction. Therefore, a hollow-like feature will be left when a threading dislocation ends on crystal surface. In this study, due to the high absorption effect of zinc oxide, which means x-ray intensity will decrease a lot in traversing the crystal, few topographic images with high contrast could be get in transmission geometry; and in grazing geometry, the images blurs when synchrotron white x-ray beam is applied. For crystals with high absorption coefficient like zinc oxide, monochromatic x-ray beam is used to taken topographic images in grazing geometry. Monochromatic XRT means, if the white synchrotron beam passes through a monochromator, an X-ray topograph is created when the sample crystal is set to the Bragg angle for a specific set of lattice planes for the selected X-ray energy. Images from different atomic planes are acquired by orienting the sample to satisfy the Bragg condition for those planes and orienting the detector to the new scattering angle to record the image. With monochromatic radiation only one topograph is recorded at a time, but the experimenter controls the energy or wavelength of the X-ray beam, the X-ray collimation, the energy or wavelength spread of the X-ray beam, and the size of the incident beam on the sample crystal. However, it is very difficult to interpret the x-ray topographs merely by information gathered by monochromatic x-ray beam. Ray tracing simulation has shown to be a very straightforward yet powerful way to interpret threading dislocation features in grazing geometry. Extensive comparisons between experiment and simulation have indicated that orientation contrast is dominant in topographs of zinc oxide. Therefore, ray-tracing simulation based on orientation contrast mechanism provides an excellent model to qualitatively and quantitatively interpret the topographic observations of dislocations in zinc oxide.

The technique was firstly proposed by X. Huang and got further development by Y. Chen and F. Wu[13] for various dislocations in SiC. The schematic of ray-tracing simulation is shown in Fig. 11.
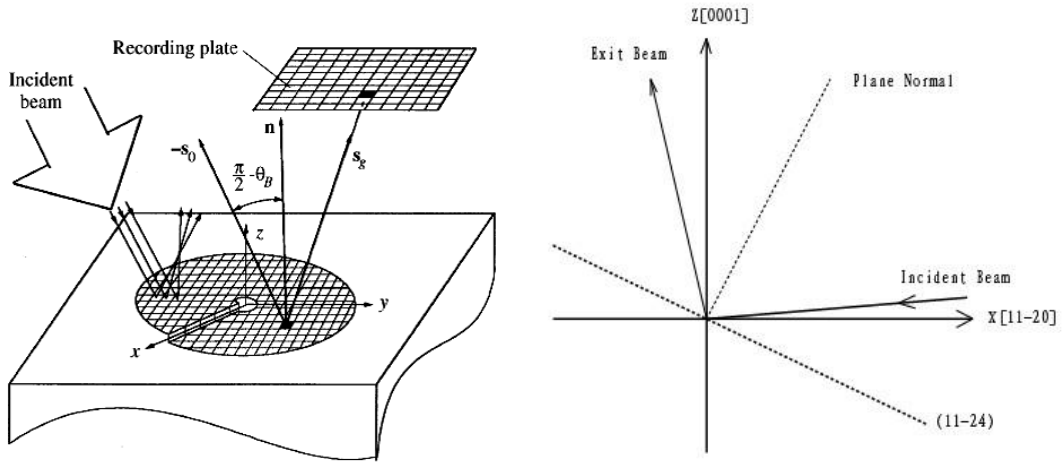
Figure 11: Schematic of ray tracing simulation[14]   **Figure 12:** Coordinate system in simulation work

The simulation work is carried out using Wolfram Mathematica 8.0 software. In the simulation process, an appropriate coordinate system could not only simplify calculation process but also accelerate program efficiency; therefore, it is of great importance to select the coordinate system. In this study, the coordinate origin is set in the dislocation center; x-axis is set to be parallel to [11-20]; z-axis is set to be parallel to [0001]; y-axis is set to have the direction of [-1100], which points inward the paper-plane. The system is shown in Fig. 12.

Once the coordinate system is settled, vectors of reflection plane, incident beam, plane normal, exit beam and film plane have to be carefully calculated. For example, as we have already known that there is no off-cut in the sample and the surface plane is (0001) and incident angle is 2 degree, the vector of incident beam $\overrightarrow{s_0}$ is [-cos2°,0,-sin2°]. (11-24) reflection is the plane we choose to find the features of each dislocation for zinc oxide's 2H structure. The angle between the surface plane (0001) and plane (11-24) could be calculated from the codes:

$Please\ input\ the\ parameters\ of\ the\ lattice;$
$a = 3.2426; b = 3.2426; c = 5.1948;$
$\alpha = \pi/2 ; \beta = \pi/2 ; \gamma = 2\pi/3 ;$
$Please\ input\ the\ parameters\ of\ the\ planes;$
$H1 = 0; K1 = 0; L1 = 1;$
$H2 = 1; K2 = 1; L2 = 4;$
$V = a * b * c * (1 - (Cos[\alpha])^2 - (Cos[\beta])^2 - (Cos[\gamma])^2 + 2 * Cos[\alpha] * Cos[\beta] * Cos[\gamma])^{0.5};$
$d = b * c * Sin[\alpha]/V ;$
$e = c * a * Sin[\beta]/V ;$
$f = a * b * Sin[\gamma]/V ;$
$A = (Cos[\beta] * Cos[\gamma] - Cos[\alpha])/(Sin[\beta] * Sin[\gamma]) ;$

$B = (Cos[\gamma] * Cos[\alpha] - Cos[\beta])/(Sin[\gamma] * Sin[\alpha]);$
$F = (Cos[\alpha] * Cos[\beta] - Cos[\gamma])/(Sin[\alpha] * Sin[\beta]);$

$$X = V^{-1} * (H1^\wedge2 * b^\wedge2 * c^\wedge2 * (Sin[\alpha])^\wedge2 + K1^\wedge2 * c^\wedge2 * a^\wedge2 * (Sin[\beta])^\wedge2 + L1^\wedge2$$
$$* a^\wedge2 * b^\wedge2 * (Sin[\gamma])^\wedge2 + 2 * K1 * L1 * a^\wedge2 * b * c * (Cos[\beta] * Cos[\gamma]$$
$$- Cos[\alpha]) + 2 * L1 * H1 * a * b^\wedge2 * c * (Cos[\gamma] * Cos[\alpha] - Cos[\beta]) + 2$$
$$* H1 * K1 * a * b * c^\wedge2 * (Cos[\alpha] * Cos[\beta] - Cos[\gamma]))^\wedge0.5;$$

$$Y = V^{-1} * \big(H2^2 * b^2 * c^2 * (Sin[\alpha])^2 + K2^2 * c^2 * a^2 * (Sin[\beta])^2 + L2^2 * a^2 * b^2$$
$$* (Sin[\gamma])^2 + 2 * K2 * L2 * a^2 * b * c * (Cos[\beta] * Cos[\gamma] - Cos[\alpha]) + 2$$
$$* L2 * H2 * a * b^2 * c * (Cos[\gamma] * Cos[\alpha] - Cos[\beta]) + 2 * H2 * K2 * a * b$$
$$* c^2 * (Cos[\alpha] * Cos[\beta] - Cos[\gamma])\big)^{0.5};$$

$$\varphi = ArcCos \left[X^{-1} * Y^{-1} \right.$$
$$\left. * \begin{pmatrix} H1 * H2 * d^2 + K1 * K2 * e^2 + L1 * L2 * f^2 + \\ (K1 * L2 + K2 * L1) * e * f * A + (H1 * L2 + H2 * L1) * f * d * B + \\ (H1 * K2 + H2 * K1) * d * c * F \end{pmatrix} \right]$$

The film is set to be perpendicular to the exit beam before distortion, and the distance between film and sample is about 15-20cm. The distance value would not play an important role in simulation. The next step is to set up a matrix to store the intensity map of the diffracted beam. In the simulation process, the sample surface is divided into small squares with constant area, as shown in Fig.11. Also, the area division for film is applied. In Mathematica, the idea of matrix is introduced to make those area divisions come into truth. The number of diffracted beam that hits onto each square on film is counted and therefore, a matrix with the stress information on sample is generated. The number of elements in this matrix decides the resolution of the simulated image. The resolution is selected in such a way that a) the resolution is not too low and b) there are not too many elements in the matrix so that the simulation takes extremely long. Normally a 500×500 matrix is used. Note that the matrix density map has to be set in the same orientation as we view the film.

We have proved the truth of $\vec{n} = \vec{n_0} - \nabla(\vec{n_0} \cdot \vec{u})$, which could be used to get plane normal after distortion $\vec{n}$ once the displacement field $\vec{u}$ is known. The diffracted beam vector can be calculated based on the equation $\vec{s_0} \times \vec{n} = -\vec{n} \times \vec{s}$, where $\vec{s_0}$ is the incident beam vector. The equation $\vec{s_0} \times \vec{n} = -\vec{n} \times \vec{s}$ could be easily deduced from the diffraction geometry. In our simulation, we assume an ideal plane wave and the wave vector of the incidence beam is fixed. The intensity distribution on the x-ray film can be mapped by calculating the wave vector of each diffracted beam from each small area defined on the crystal surface. Therefore, the dislocation image, which is actually a mapping of the diffracted beam intensity, can be simulated.

2.5 Experiment

Commercial *c*-plane ZnO wafers grown by the hydrothermal method were initially imaged in the transmission geometry to characterize defects in the bulk. 11-24 reflection was recorded in grazing geometry with 2 °incident angle to image threading defects. Synchrotron white beam X-ray topography experiments were carried out at the Stony Brook Synchrotron Topography Station, Beamline X-19C, at the National Synchrotron Light Source while synchrotron monochromatic X-ray topography experiments were carried out at the Advanced Photon Source, Beamline XOR-33BM/UNI-CAT. The direct white beam from the storage ring is used at the NSLS and the maximum beam size at the sample is approximately 7×40 mm². The vertical divergence angle is $mc_2/E \approx 0.18$ mrad (*m* is the mass of the electron, *c* is the velocity of the light and *E* is the electron energy). In APS, the white beam is mono-chromatized by two cooled parallel Si(111) crystals and the x-ray energy is tunable between 2.4 – 40 keV. All images were recorded on Agfa Structurix D3-SC films. Ray tracing simulation work is carried out using Wolfram Mathematica 8.0 software. Settings in BNL and APS are illustrated in Fig. 9.
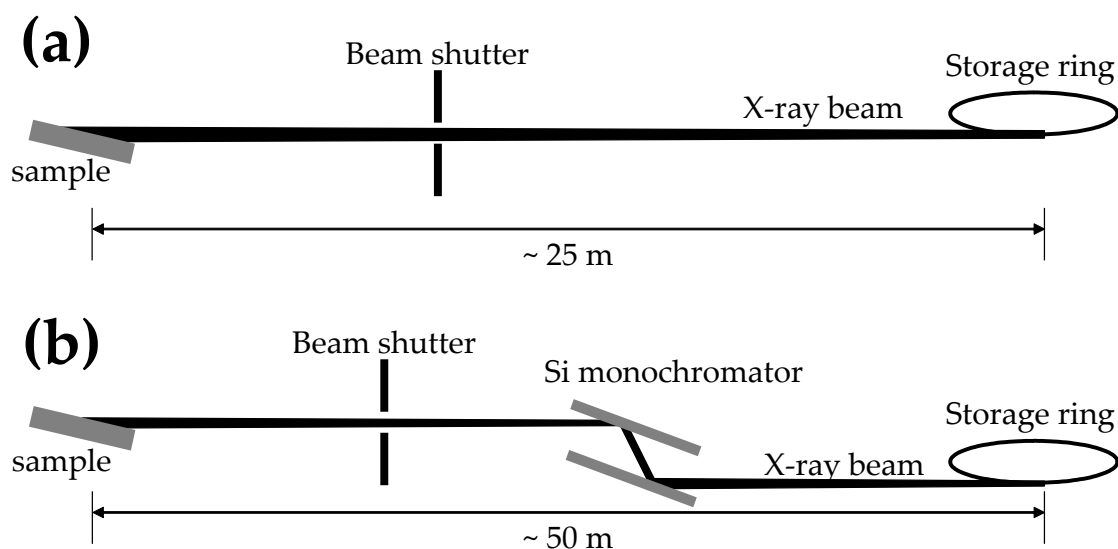
Figure 13: Schematics of experimental setting-ups at NSLS (a) and APS (b)

2.6 Results and Discussion

An overview of defects in hydrothermal grown zinc oxide substrates is shown in Fig. 10. In general, there are mainly two kinds of dislocations: growth dislocation and stress induced dislocation. Growth dislocations are observed in crystals grown from vapor, melt, solution and flux. They are formed during the growth process. Multiple growth dislocation origins have been observed: (a) the continuation of dislocations already present in the seed; (b) the relaxation of stresses arising from handling damage on the surface of the seed; (c) the

relaxation of stresses arising from the incorporation of inclusions of solvent or impurity which can occur on the seed surface or later during growth which can equivalently be viewed as imperfect lattice closure around such inclusions; (d) the relaxation of stresses arising from coalescence between two or more mis-oriented growth centers. As for stress-induced dislocations in this study, they are usually formed on basal plane (0001) or on prismatic planes nucleating from boule edges due to thermal gradient stress, with Burger's vector 1/3<11-20>. Also, there exist some dislocations pairs nucleated from inclusions incorporated into crystals.
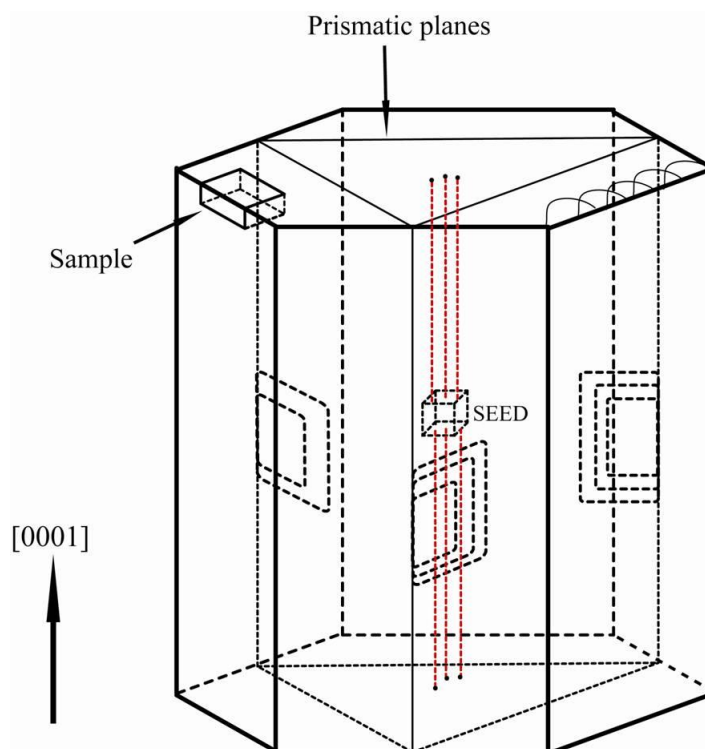
Figure 14: Overview of defects in hydrothermal grown ZnO substrates, seed is in the center of boule; red dashed lines are dislocations propagated from seed; dislocation loops on (0001) basal plane and prismatic planes are stress-induced dislocations; sample in this study is one part of (0001) plane cut wafer, without offcuts (may contain seed).

Theoretically, there are 2 possible threading screw dislocations (assume n equal 1), 6 possible threading edge dislocations and 12 possible $c+a$ dislocations for the basal plane cut wurtzite ZnO crystal. The diffraction vector for all these dislocations is $[11\bar{2}4]$, pointing upwards in simulated images. The a-component is defined in such way that 1/3[1-20] is the reference direction, referred to as 0 °a which is 0 °to the g vector, 1/3[$2\bar{1}\bar{1}0$] is 60 °a which is 60 °to the g vector, and so on, as shown in Fig. 9. For example, $c+0°a$ means, the c-component's Burgers vector is [0001] and the a-component's Burgers vector is $1/3[11\bar{2}0]$. Simulation results of the contrast of all 20 threading dislocations with c-component or a-component of Burgers vector in 11-24 grazing-incidence topographs are shown in Fig. 16-18.

1/3<11$\bar{2}$0>0°a

1/3<$\bar{1}$2$\bar{1}$0> 300°a   1/3<2$\bar{1}\bar{1}$0> 60°a

1/3<$\bar{2}$110> 240°a   1/3<1$\bar{2}$10> 120°a

1/3<$\bar{1}\bar{1}$20> 180°a

G=11-24
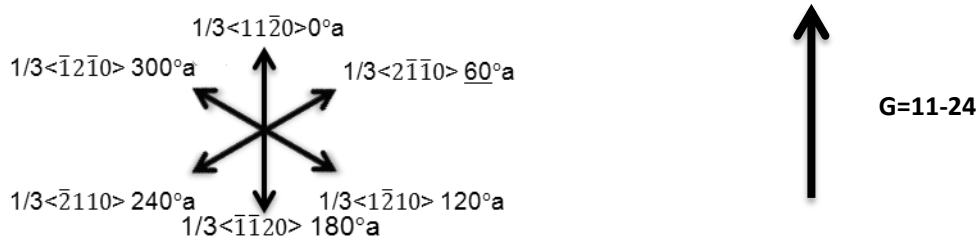
Figure 15: Directions of Burgers vectors of *a*-components.

Two possible threading screw dislocations:

 [0001]   [000$\bar{1}$]
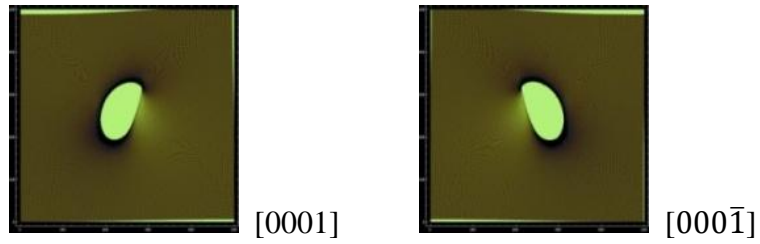
Figure 16: Simulated threading screw dislocations

Twelve possible c+a dislocations:

 c+0°a   c+60°a   c+120°a

 c+180°a   c+240°a   c+300°a

 -c+0°a   -c+60°a   -c+120°a

 -c+180°a   -c+240°a   -c+300°a
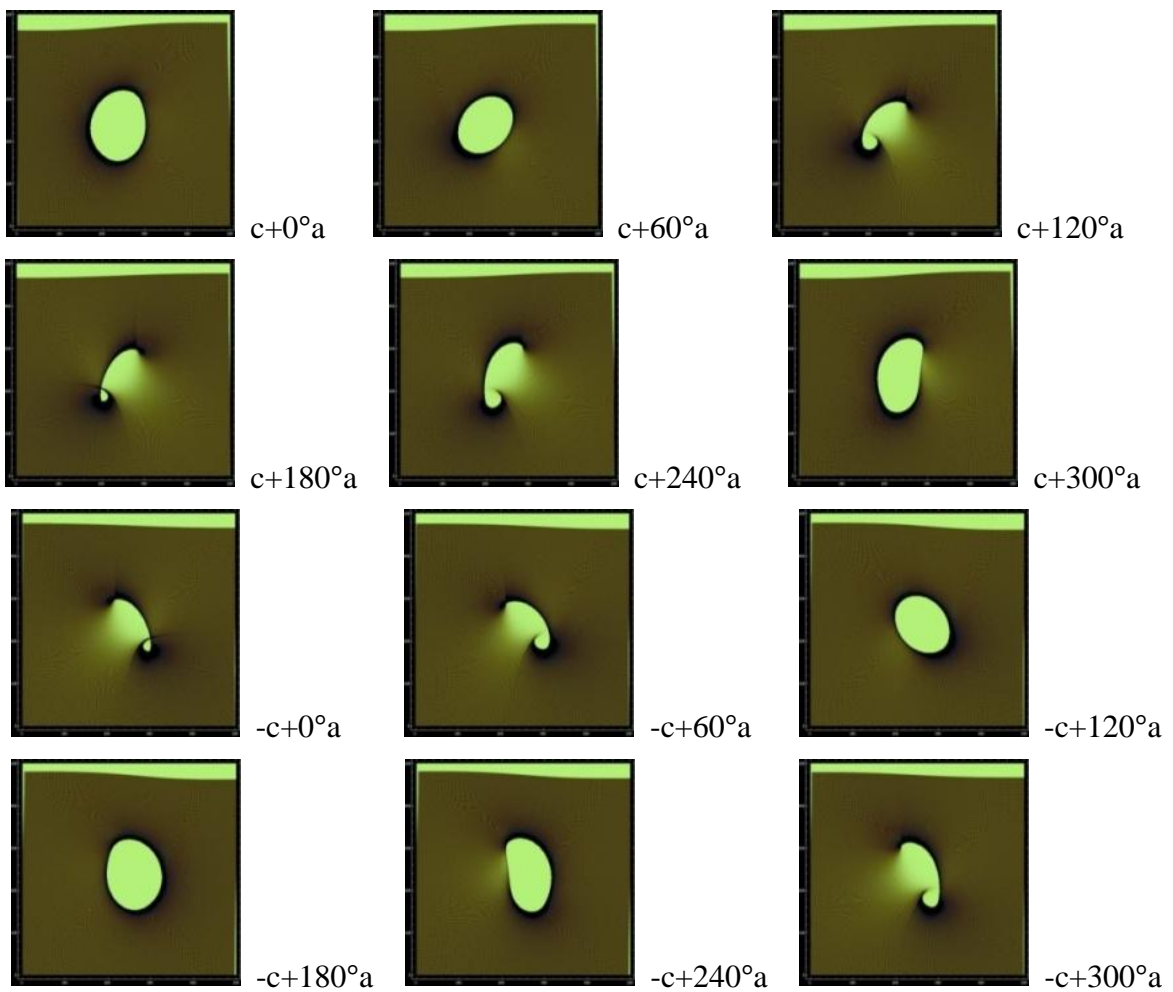
Figure 17: Simulated c+a dislocations

Six Possible Threading edge dislocations:

1/3[11$\bar{2}$0]

1/3[2$\bar{1}\bar{1}$0]

1/3[1$\bar{2}$10]

1/3[$\bar{1}\bar{1}$20]

1/3[$\bar{2}$110]

1/3[$\bar{1}$2$\bar{1}$0]
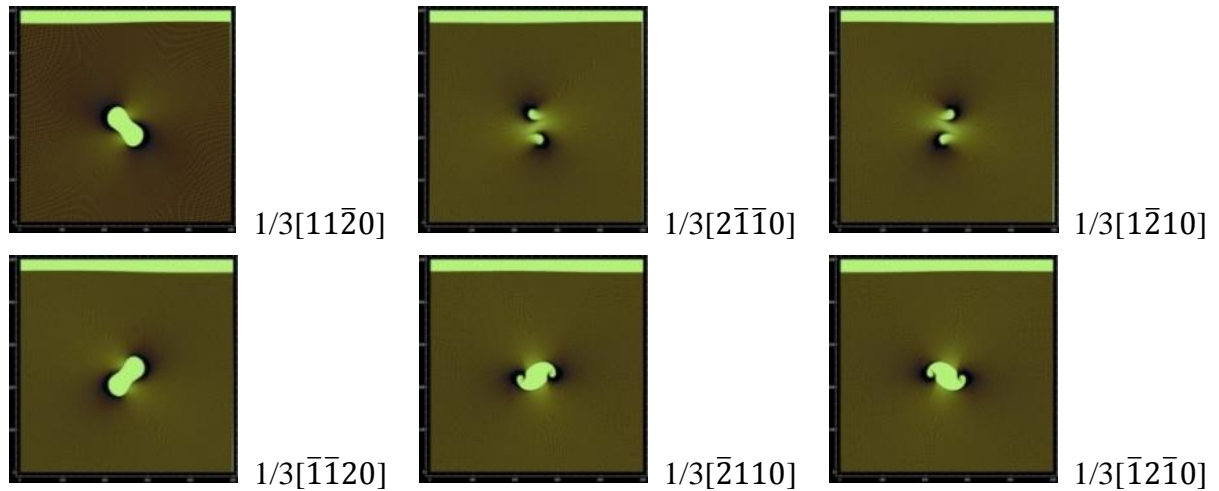
Figure 18: Simulated threading edge dislocations

Generally speaking, the contrast pattern contains a white and tilted elliptical spot in the center and a black perimeter surrounding the spot. The contrast pattern can be divided into two groups according to the tilt direction of the ellipse. When the *c*-component of Burgers vector is positive, the ellipses are tilted to the right; when the *c*-component of Burgers vector is negative, the ellipses are tilted to the left. For threading edge dislocations, the contrast pattern seems to contain two dislocation cores, tilting different angels to each other; and in two cases, the two cores get separated.

(a)

(b)

(c)
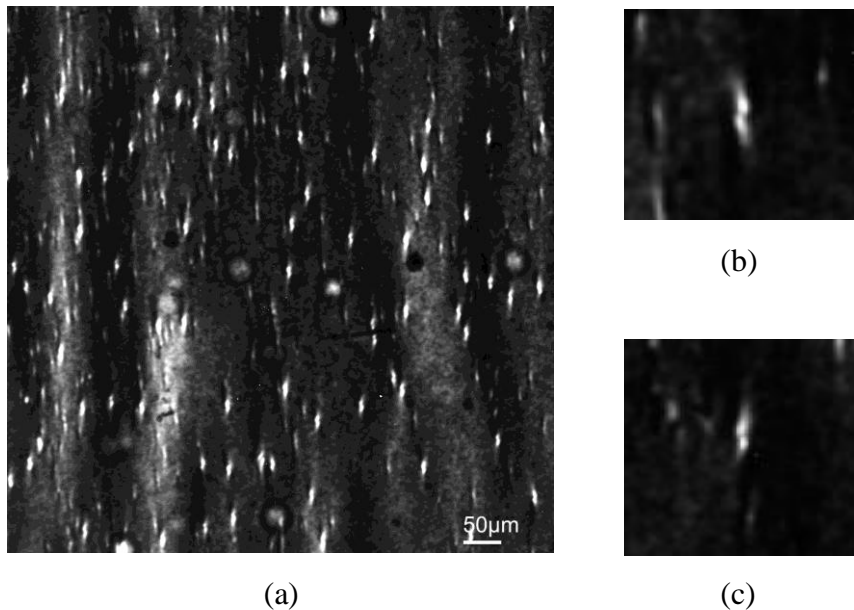
Figure 19: Monochromatic grazing incidence X-ray topograph showing contrast from chiefly two types of TEDs with Burgers vectors $1/3\,[1\bar{2}10]$ (b) and $1/3\,[2\bar{1}\bar{1}0]$ (c).

Detailed studies of grazing incidence monochromatic X-ray topographs from multiple

24

ZnO wafers reveal no contrast features matched to TSD or $c+a$ simulated images. This means, few c-component dislocations are present in this sample. Most dislocation features we observed in this study are TEDs with Burgers vector of either $1/3\,[2\bar{1}\bar{1}0]$ or $1/3\,[1\bar{2}10]$, while very few other type TEDs could be found from the topographic images (see Fig. 19).

X-ray topography in the transmission geometry on these ZnO wafers reveal defects in the entire bulk of the crystal wafers. Topograph from a typical wafer (Fig. 20(a)) reveals criss-crossed patterns of prismatic slip bands (S) running along the $\langle 11\bar{2}0\rangle$ directions and inhomogeneously scattered inclusions (I). Prismatic slip on all three prism planes is observed but predominantly of the $[1\bar{2}10]$ on $(10\bar{1}0)$ and $[2\bar{1}\bar{1}0]$ on $(01\bar{1}0)$ types. The slip bands are composed of dislocation half-loops with long screw segments (horizontal red dashed lines) extending into the wafer with short edge segments (vertical red dashed lines) at the ends (see Fig. 22(a) for schematic). The prismatic slip dislocations exhibit the phenomenon of cross-slip (see Fig.20(b)) where the screw segments of dislocation half-loops lying in the prismatic planes have cross-slipped onto the basal plane. Fig. 21 shows the detailed process of cross slip.
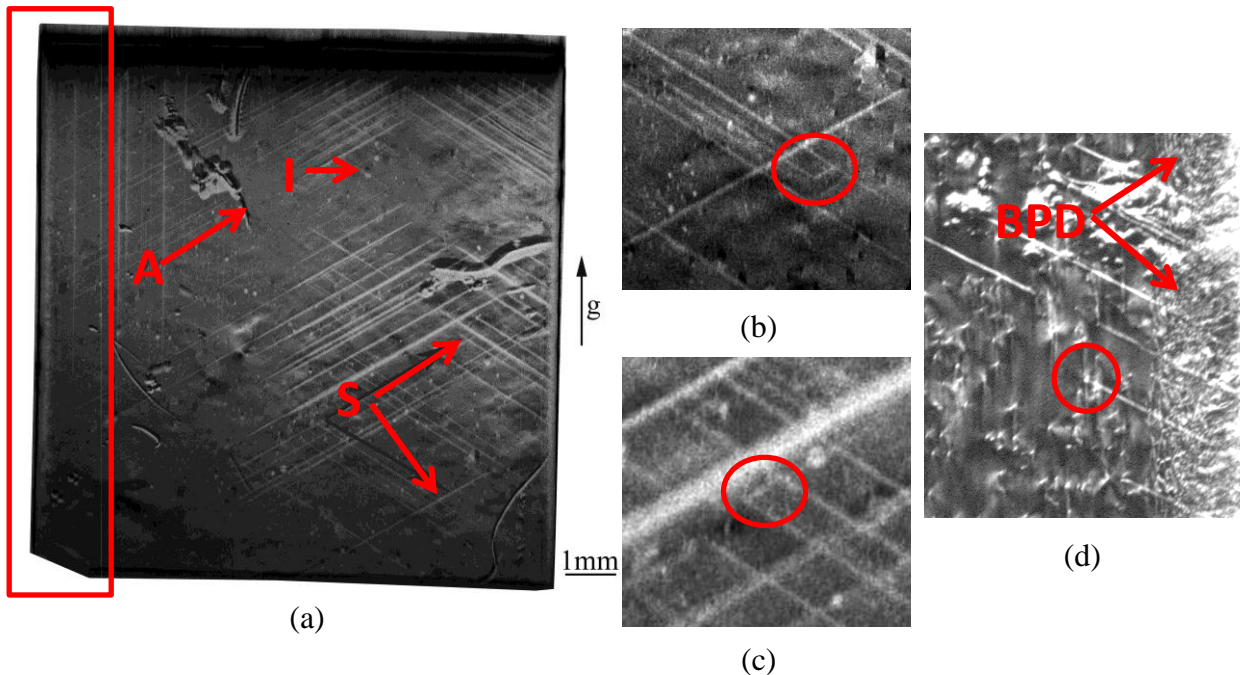
Figure 20: (a) White beam transmission topograph of a typical ZnO wafer showing prismatic slip bands (S), inclusions (I) and surface artifacts (A); (b) & (c) High magnification topographs showing the cross-slip of screw segments on to the basal plane (inside circle); (d) Monochromatic topograph showing TED images at the end of prismatic slip bands (inside circle) and BPD loops nucleated from wafer edge.

Closer examination of the wafer edges reveals a dense concentration of basal plane dislocation half-loops nucleated from the edges. High magnification monochromatic topograph (Fig. 20(d)) reveals these loops in greater detail. These loops are most likely produced during the cutting process, while the prismatic loops are mainly post-growth thermal-stress induced dislocations. The monochromatic topograph also reveals that the ends

of the prismatic slip bands are associated with a TED contrast (Fig. 20(d)).
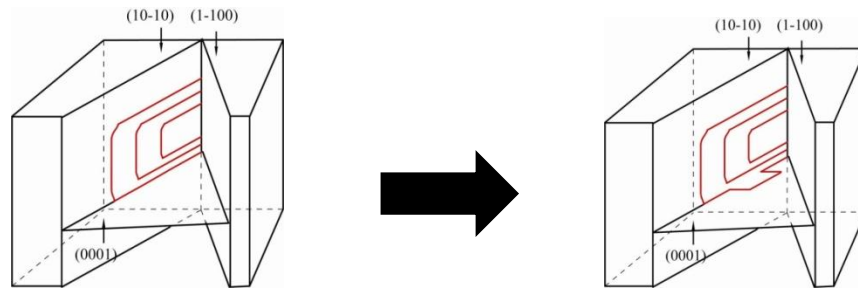
Figure 21: Schematic of cross slip on basal planes

From these observations, a clear picture of the origin of TED contrast is obtained. When the c-plane wafer is cut from the boule, the predominantly $[1\bar{2}10]$ and $[2\bar{1}\bar{1}0]$ prismatic dislocation loops can be cut in the middle perpendicular to the edge segments. Therefore, the edge segments intersect the surface nearly along c-axis and appear as TEDs on the intersection plane which is the surface plane in this study (see Fig. 22 for schematic).

The dislocation density of these two TED types is approximately $2.88 \times 10^4/cm^2$ near the wafer edges, and they take up about 50% of all threading dislocations in the $11\bar{2}4$ reflection. In the central part, the minimum dislocation density is about $800/cm^2$. The remaining features on the grazing incidence topographic images are BPDs basal plane dislocations, which appear as a light straight white line, and inclusions which appear as circles of white contrast. Their density is $4.89 \times 10^4/cm^2$. Note that the BPDs usually do not terminate on the crystal surface; therefore, they will not strongly influence the structural quality of the epilayer grown on it; while threading dislocations which will propagate into the device grown on the substrates are more damaging.

(a) (b)
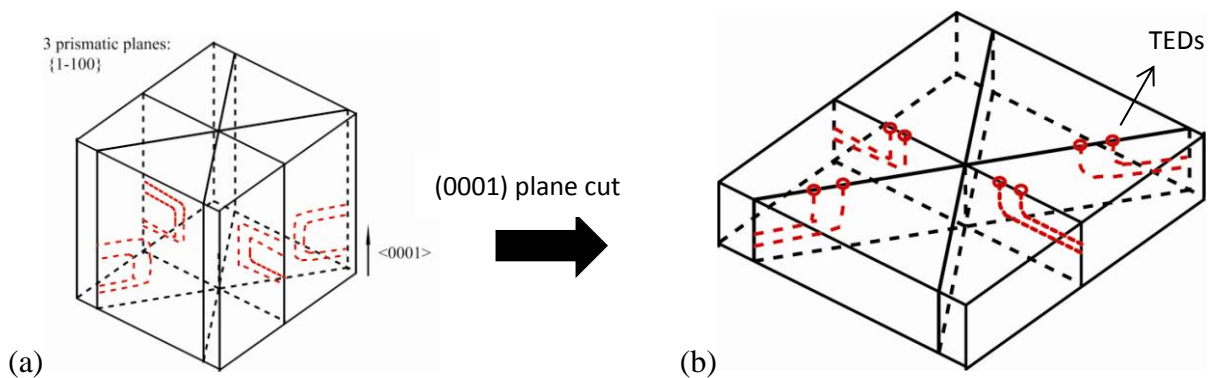
Figure 22: Schematic of the origin of TEDs on c-plane cut wafer (a) Prismatic loops generated in boule due to thermal gradient induced stresses. (b) Wafer slicing perpendicular to edge segments resulting in TEDs on surface.

Moreover, if we blow up the edge part of the transmission image in Fig. 20(a), large quantity of dislocation loops are observed in this area. Detailed characterization shows that they are stress induced screw dislocations with the burgers vector of 1/3<11-20> and they slip on the basal plane, which is (0001) plane. Usually, this kind of dislocations will dissociated into Shockley partials separated by a Shockley fault; but it did not happen in this

study. These dislocations nucleate primarily in the highly strained outer regions of the boule and become mobile and expand toward the interior of the boule under the action of shear stresses on the basal plane. The dislocation originates from the outer regions most probably arises from differential thermal expansion effects between polycrystalline and polytype inclusions leading to the generation of further shear stress concentrations. Figure 23(a) and (b) show a transmission topograph recorded with synchrotron radiation. Analysis of the white contrast associated with all of the approximately concentric half-loops expanding towards the interior of the wafer (based on the ray-tracing principle) demonstrates that they are all of the same sign, consistent with the prediction before.

| (a) | (b) | (c) |
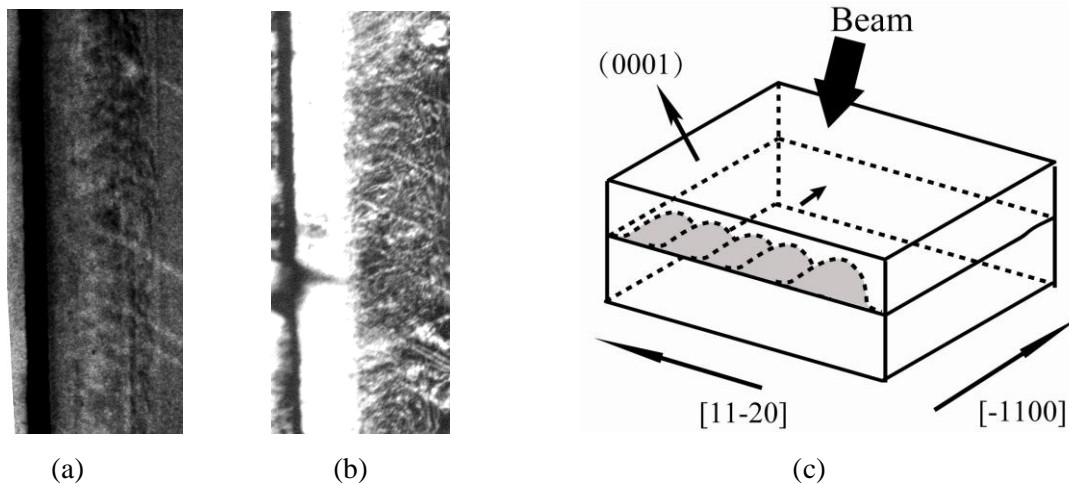
Figure 23: Dislocation loops nucleating in the edge region in two different samples (a) and (b); schematic of dislocation loops (c)

2.7 Conclusions

ZnO substrates grown by hydrothermal method are characterized by prismatic slip bands and inclusions with basal dislocations concentrated near edges. Ray tracing simulation is successfully used in interpreting the Burgers vectors of threading dislocations in $11\bar{2}4$ grazing incidence reflection topographs. TEDs whose Burgers vectors are $1/3\,[2\bar{1}\bar{1}0]$ and $1/3\,[1\bar{2}10]$ are generally found. These are edge segments of prismatic loops. Threading screw dislocations or $c+a$ dislocations are not observed. The overall dislocation density for hydrothermal grown ZnO is 5000/cm^2. To minimize threading dislocations in the sample, prismatic slip must be eliminated by minimizing thermal gradient stresses.

Chapter III. Residue Stress Mapping and Depth Profiling via Ray Tracing in Packaged Silicon Circuits

3.1 Introduction

Semiconductor devices are becoming increasingly more complex as the number of transistors increases in the same Integrated Circuit (IC) area. Due to the complexity in design; processing and packaging of the device plays a crucial role in the IC fabrication. Package induced residual stress are Residual stresses are known to cause instability in electrical performance and eventually kill the device if the material yields to produce dislocation[15,16]. Various techniques have been used to determine residue stress in crystals[17,18,19]. V. Sarkar and Y. Chen have developed a novel technique (SMART) based on ray tracing to non-destructively and non-invasively map the complete stress tensor as a function of three dimensional positions in any single crystal bulk material. This method uses the technique of x-ray topography in combination with a fine-scale mesh/grating/reticule, otherwise referred to as synchrotron white beam x-ray reticulography (SWBXR), followed by detailed image analysis and calculation enabling determination of all stress components.

As shown in Chaper I, there exists a relationship between the stress state in a crystal and the local lattice plane orientation, which is $\vec{n} = \vec{n_0} - \nabla(\vec{n_0} \cdot \vec{u})$, and that this relationship can be exploited in order to determine the full strain tensor as a function of position inside the crystal. Then, the elastic constants of the sample could be utilized to convert strain into stress values. A grid is used to trace exit x-ray beams from the sample. The grid essentially breaks the area-filling X-ray beam into an array of micro-beams, each micro-beam is then traced separately. The results of such measurements carried out using three independent x-ray reflections can be input into the mathematical relationship between the strain tensor and the local lattice plane orientation allowing calculation of the complete strain tensor as a function of lateral position in the crystal. Vish[20] has successfully applied this technique to silicon circuits in transmission geometry to get stress values in bulk material. This method has a unique advantage compared with other stress measurement technique in that it can evaluate all six components of the complete stress tensor in a nondestructive way. In this study, stress and depth profiling is measured with SMART, associated with penetration depth, in grazing geometry; and 3D stress map is generated.

Vish also conducted a lot of research on depth profiling[21], but there exist some errors in his assumption. In this study, we try to correct those assumptions to get stress values which are closest to the real ones.

3.2 Proof of SMART

The equation $\vec{n} = \vec{n_0} - \nabla(\vec{n_0} \cdot \vec{u})$ provides the theoretical basis for SMART. This provides the analysis methodology which enables the determination of the full stress tensor as a function of 3D position in the crystal. The schematic of strain measurement in this study is shown in Fig. 24. D is the position where diffracted beam hits on the film under stress free situation; D' is the position where diffracted beam hits on the film in experiment. Therefore, plane normal before and after distortion could be calculated. Using the equation $\vec{n} = \vec{n_0} - \nabla(\vec{n_0} \cdot \vec{u})$, strain distribution on the sample is generated. According to Hooke's law, the relationship between stress and strain can be written in contracted notation as

$$\sigma_{ij} = C_{ijkl}\varepsilon_{kl} \qquad i,j = 1,2,\ldots,6$$

where σ_i are the stress components, C_{ij} is the stiffness matrix, and ε_j are the strain components.
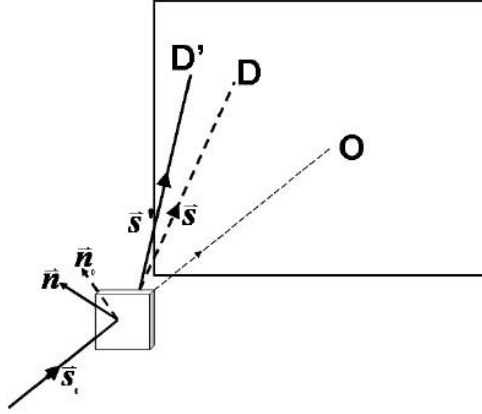
Figure 24: Strain measurement in SMART

In 3-dimension situations, the equation $\vec{n} = \vec{n_0} - \nabla(\vec{n_0} \cdot \vec{u})$ is written as:

$$\vec{n}(x,y,z) = \vec{n_0}(x,y,z) - \nabla[\vec{n_0}(x,y,z) \cdot \vec{u}(x,y,z)]$$

where $\vec{n}(x,y,z) = n_x\vec{\imath} + n_y\vec{\jmath} + n_z\vec{k}$ is the plane normal at (x,y,z) after distortion;

$\vec{n_0}(x,y,z) = n_{0x}\vec{\imath} + n_{0y}\vec{\jmath} + n_{0z}\vec{k}$ is the plane normal at (x,y,z) before distortion;

$\vec{u}(x,y,z) = u_x\vec{\imath} + u_y\vec{\jmath} + u_z\vec{k}$ is the displacement at (x,y,z).

Also, at point (x,y,z), the equation could be split into 3 sub-equations:

$$n_x = n_x^0 - (n_x^0 \frac{\partial u_x}{\partial x} + n_y^0 \frac{\partial u_y}{\partial x} + n_z^0 \frac{\partial u_z}{\partial x})$$

$$n_y = n_y^0 - \left(n_x^0 \frac{\partial u_x}{\partial y} + n_y^0 \frac{\partial u_y}{\partial y} + n_z^0 \frac{\partial u_z}{\partial y}\right)$$

$$n_z = n_z^0 - (n_x^0 \frac{\partial u_x}{\partial z} + n_y^0 \frac{\partial u_y}{\partial z} + n_z^0 \frac{\partial u_z}{\partial z})$$

To solve one equation like $n_x = n_x^0 - (n_x^0 \frac{\partial u_x}{\partial x} + n_y^0 \frac{\partial u_y}{\partial x} + n_z^0 \frac{\partial u_z}{\partial x})$, three groups of n_x,

n_x^0, n_y^0, n_z^0 have to be provided for there are three undetermined parameters in the equations.

Therefore, in SMART, information from three diffraction spot has to be collected. A set of equations are:

$$n_{x1} = n_{x1}^0 - (n_{x1}^0 \frac{\partial u_x}{\partial x} + n_{y1}^0 \frac{\partial u_y}{\partial x} + n_{z1}^0 \frac{\partial u_z}{\partial x})$$

$$n_{x2} = n_{x2}^0 - (n_{x2}^0 \frac{\partial u_x}{\partial x} + n_{y2}^0 \frac{\partial u_y}{\partial x} + n_{z2}^0 \frac{\partial u_z}{\partial x})$$

$$n_{x3} = n_{x3}^0 - (n_{x3}^0 \frac{\partial u_x}{\partial x} + n_{y3}^0 \frac{\partial u_y}{\partial x} + n_{z3}^0 \frac{\partial u_z}{\partial x})$$

From these three equations, we can get the value of $\frac{\partial u_x}{\partial x}, \frac{\partial u_y}{\partial x}, \frac{\partial u_z}{\partial x}$.

$$n_{y1} = n_{y1}^0 - (n_{x1}^0 \frac{\partial u_x}{\partial y} + n_{y1}^0 \frac{\partial u_y}{\partial y} + n_{z1}^0 \frac{\partial u_z}{\partial y})$$

$$n_{y2} = n_{y2}^0 - (n_{x2}^0 \frac{\partial u_x}{\partial y} + n_{y2}^0 \frac{\partial u_y}{\partial y} + n_{z2}^0 \frac{\partial u_z}{\partial y})$$

$$n_{y3} = n_{y3}^0 - (n_{x3}^0 \frac{\partial u_x}{\partial y} + n_{y3}^0 \frac{\partial u_y}{\partial y} + n_{z3}^0 \frac{\partial u_z}{\partial y})$$

From these three equations, we can get the value of $\frac{\partial u_x}{\partial y}, \frac{\partial u_y}{\partial y}, \frac{\partial u_z}{\partial y}$.

$$n_{z1} = n_{z1}^0 - (n_{x1}^0 \frac{\partial u_x}{\partial z} + n_{y1}^0 \frac{\partial u_y}{\partial z} + n_{z1}^0 \frac{\partial u_z}{\partial z})$$

$$n_{z2} = n_{z2}^0 - (n_{x2}^0 \frac{\partial u_x}{\partial z} + n_{y2}^0 \frac{\partial u_y}{\partial z} + n_{z2}^0 \frac{\partial u_z}{\partial z})$$

$$n_{z3} = n_{z3}^0 - (n_{x3}^0 \frac{\partial u_x}{\partial z} + n_{y3}^0 \frac{\partial u_y}{\partial z} + n_{z3}^0 \frac{\partial u_z}{\partial z})$$

From these three equations, we can get the value of $\frac{\partial u_x}{\partial z}, \frac{\partial u_y}{\partial z}, \frac{\partial u_z}{\partial z}$.

As the value of $\frac{\partial u_x}{\partial x}, \frac{\partial u_y}{\partial x}, \frac{\partial u_z}{\partial x}, \frac{\partial u_x}{\partial y}, \frac{\partial u_y}{\partial y}, \frac{\partial u_z}{\partial y}, \frac{\partial u_x}{\partial z}, \frac{\partial u_y}{\partial z}, \frac{\partial u_z}{\partial z}$ are obtained, pure strain tensor could be derived as:

$$\varepsilon_{ij} = \frac{1}{2}\left(\frac{\partial u_i}{\partial j} + \frac{\partial u_j}{\partial i}\right) = \begin{bmatrix} \varepsilon_{xx} & \varepsilon_{xy} & \varepsilon_{xz} \\ \varepsilon_{yx} & \varepsilon_{yy} & \varepsilon_{yz} \\ \varepsilon_{zx} & \varepsilon_{zy} & \varepsilon_{zz} \end{bmatrix}$$

$$= \begin{bmatrix} \dfrac{\partial u_x}{\partial x} & \dfrac{1}{2}(\dfrac{\partial u_x}{\partial y} + \dfrac{\partial u_y}{\partial x}) & \dfrac{1}{2}(\dfrac{\partial u_x}{\partial z} + \dfrac{\partial u_z}{\partial x}) \\ \dfrac{1}{2}(\dfrac{\partial u_x}{\partial y} + \dfrac{\partial u_y}{\partial x}) & \dfrac{\partial u_y}{\partial y} & \dfrac{1}{2}(\dfrac{\partial u_y}{\partial z} + \dfrac{\partial u_z}{\partial y}) \\ \dfrac{1}{2}(\dfrac{\partial u_x}{\partial z} + \dfrac{\partial u_z}{\partial x}) & \dfrac{1}{2}(\dfrac{\partial u_y}{\partial z} + \dfrac{\partial u_z}{\partial y}) & \dfrac{\partial u_z}{\partial z} \end{bmatrix}$$

Subsequently, the strains can be converted to stresses using the crystal's elastic constants.

Vish has proved that in transmission geometry, same results are obtained by choice of any three randomly selected reticulographs. But in this study, because the concept of penetration depth is commonly used, which is strongly influenced by different reticulographs, we cannot select three diffraction spot randomly. We have to choose three diffraction spots with the closest penetration depth to minimize errors.

Note that penetration depth is defined as the depth (t) at which intensity drops to 1/e. The direct calculation result from SMART technique is a weighted average value, which is of little use than the actual stress distributions. The reason that the stress value is weighted average and not a simple average is that the diffraction data has more information from volume which is near the surface rather than further deep into the crystal because X-ray intensity reduces exponentially as it penetrates into the crystal. In general any diffraction technique in the reflection geometry will result in a stress value which is Laplace transform of real space stress distribution given by the following equation[22,23,24]:

$$\bar{\sigma}(\tau) = \frac{1}{\tau}\mathcal{L}\left[\sigma(z), \frac{1}{\tau}\right] = \frac{1}{\tau}\int_0^{\infty} \sigma(z)e^{-\frac{z}{\tau}}dz$$

where τ is the penetration depth, z is the depth from the surface, $\bar{\sigma}(\tau)$ is the weighted average stress value which is equal to the experimentally determined stress value, $\sigma(z)$ is the real stress depth function.

Assume $s = \frac{1}{\tau}$,

$$\bar{\sigma}\left(\frac{1}{s}\right) = s\int_0^{\infty} \sigma(z)e^{-zs}dz$$

$$\frac{1}{s}\bar{\sigma}\left(\frac{1}{s}\right) = \int_0^{\infty} \sigma(z)e^{-zs}dz$$

$$\sigma(z) = \mathcal{L}^{-1}\left[\frac{1}{s}\bar{\sigma}\left(\frac{1}{s}\right), s\right]$$

All the Laplace transform and reverse Laplace transform in this study are operated by Mathematica.

3.3 Experiment

Commercial silicon sample from Intel was studied by synchrotron white beam x-ray topography in grazing geometry in National Synchrotron Light Source X19C located at Brookhaven National Laboratory. Multiple images were recorded by varying the incident angle in steps of 1 degree. A fine scale tungsten grid, described in Fig. 26, is placed just above and parallel to the sample surface. Spacing between the bars in the grid is 508μm and bar width is 102μm. Depth profiles are calculated at locations beneath the surface of the crystal at points defined by the grid-bar intersection locations. It should be noted here that the spatial resolution of this technique is solely depends on the spacing between the bars in the grid. A finer grid (having higher price) will provide better spatial resolution. Incident X-ray beam after interacting with the crystal up to certain depth (penetration depth) diffracts in certain direction governed by Bragg's law. Diffracted beam after passing through the tungsten grid forms an image on the photographic film (Agfa structurix D3-SC) which essentially is the shadow or the inverse image of the grid. Reticulographic images were recorded using Agfa Structurix D3-SC photographic film. The schematic of this study is shown in the following:
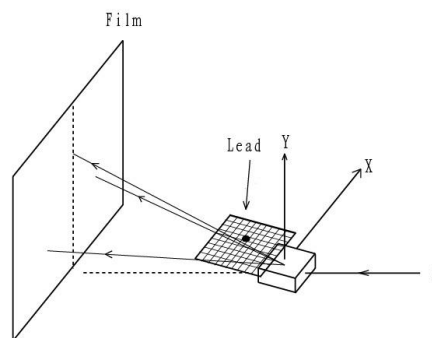
Figure 25: Schematic of SMART (lead in the center)
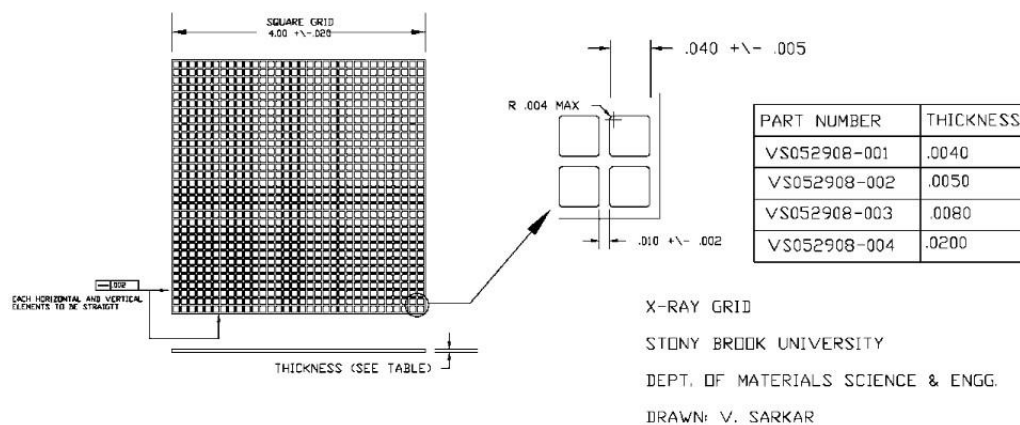
Figure 26: Engineering drawing of X-ray absorption grid used for SMART, by Vish Sarkar[25]

A small piece of lead, which has the enough size to cover one unit cell, is used to roughly locate the position of reticulographic images in the selected coordinate system. The lead should be put near the center area on the grid. Because of the strong absorption efficient of lead, the x-ray that originally goes through the unit cell now is blocked by lead. Thus on the film, a blank area could be observed, as shown in Fig. 27

.
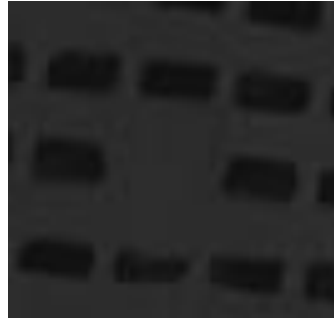
Figure 27: Blank area caused by lead in one reticulographic image

Assume the lead is set as the origin of the coordinate system on the sample; its position is therefore (0, 0, 0). Generally, we have to select three diffraction spot, and one of them is on the center axis (y-axis in this study). The blank area's position on x-axis in this reticulographic image is zero and its value on y-axis is

$$y = d \tan 2(\alpha + \beta)$$

where d is the distance between sample and film in z-axis, α is the diffraction angel and β is the rotation angel of x-axis on the sample.

Figure 28: Scan of X-ray topography film with x-axis rotating 2.3 degree

Film recorded with x-axis rotating 2.3 degrees is illustrated above. After exposure to X-rays, films are processed by developing, fixing rinsing and followed by drying. Films are scanned at a resolution of 2400 dots per inches (dpi). An electronic image file (.tiff) is generated. Image recognition software is used to detect the grid corner points in the three chosen reticulograph.

Note that in this study, the plane normal before distortion is defined instead of calculated the same way as distorted plane normal. As the angle relations are determined, the vector of one certain plane normal is also determined. Plane normal for (-22-8) reflection is defined as:

$$\text{Normal} = \begin{bmatrix} \cos c & -\sin c & 0 \\ \sin c & \cos c & 0 \\ 0 & 0 & 1 \end{bmatrix} \cdot \begin{bmatrix} \cos b & 0 & \sin b \\ 0 & 1 & 0 \\ -\sin b & 0 & \cos b \end{bmatrix} \cdot \begin{bmatrix} 1 & 0 & 0 \\ 0 & \cos a & \sin a \\ 0 & -\sin a & \cos a \end{bmatrix} \cdot \begin{bmatrix} 0 \\ 8 \\ -2^{1.5} \end{bmatrix}$$

3.4 Penetration Depth Calculation

In transmission geometry, which is used to generate stress map for bulk material, three reticulographic images could be randomly selected and it is unnecessary to index every diffraction spot and it is also unnecessary to determine the wavelength or the penetration depth of a particular reticulograph. Vish has proved the truth of this assumption. But in this study, the concept of penetration depth plays extremely important role in depth profiling; its values have to be carefully calculated. Note that penetration depth in this study is based on photoelectric absorption.

According to the program of LauePattern written by X. Huang[26], information of pattern index and geometrical location of the spot on the film could be found. These data are required for penetration depth calculation. The following picture shows the diffraction patterns which could correlate with Fig. 29.
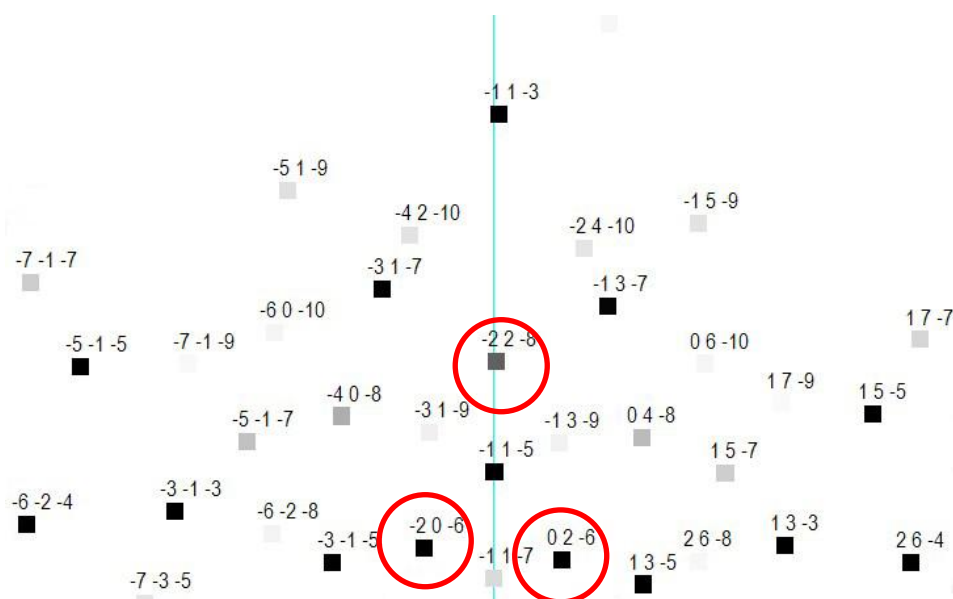
Figure 29: Diffraction patterns from LauePattern(three selected diffraction spot are marked

with red circles)

To determine the penetration depth for each reticulograph, we have to know the value of exit angel. In this study, incident angel varies from 2.3 degree to 8.3 degree with the step of 1 degree. The value of exit angle could be calculated from LauePattern. In Chapter I, we have introduced the equation for penetration depth:

$$t = \frac{1}{\mu(\frac{1}{\sin\alpha} + \frac{1}{\sin\beta})}$$

where μ is the absorption coefficient, α is the incident angle, β is the exit angle.

Assume for certain diffraction spot:
a= X coordinate of diffraction spot,
b= Y coordinate of diffraction spot,

The exit angle could be written as:

$$\phi_h = \tan^{-1}[\frac{b}{\sqrt{a^2 + sfd^2}}] - \phi_0$$

where sfd is the distance between lead and film on z-axis direction, ϕ_0 is the incident angle.

The above equation can be readily derived using geometry. All the variables on the right side of equation are known and therefore exit angle can be calculated. From LauePattern, wavelength of each diffraction spot is determined. For (-228), its wavelength is 0.4267 Å; for (-20-6) and (02-6), the value is 0.384 Å.

Mass absorption coefficient μ/ρ of silicon for the range of wavelengths 0.30~1.85 Å, with the step of 0.05Å is shown in Table. 4:

wavelength	0.30	0.35	0.40	0.45	0.50	0.55	0.60	0.65	0.70	0.75
μ/ρ	0.657	0.941	1.32	1.79	2.39	3.11	3.97	4.99	6.16	7.52
wavelength	0.80	0.85	0.90	0.95	1.00	1.05	1.10	1.15	1.20	1.25
μ/ρ	9.05	10.8	12.7	14.9	17.3	19.9	22.8	25.9	29.3	33.0
wavelength	1.30	1.35	1.40	1.45	1.50	1.55	1.60	1.65	1.70	1.85
μ/ρ	37.0	41.3	45.9	50.8	56.0	61.6	67.5	73.8	80.4	87.4

Table 4: Mass absorption coefficient of silicon

Using polynomial fitting method, the relation between absorption coefficient (assume silicon's density $\rho = 2.3290\,\text{g} \cdot cm^{-3}$) and wavelength ($\lambda$) for silicon could be determined through Mathematica:

$$u = -0.1508\lambda^6 + 1.3684\lambda^5 - 7.2723\lambda^4 + 50.179\lambda^3 - 6.6116\lambda^2 + 2.775\lambda - 0.0166$$

Therefore, penetration depth for three selected diffraction spot at different incident angle

could be calculated:

degree	-22-8	02-6	-20-6	average
2	72.1893	84.6983	85.52	80.80253
3	94.61	105.78	106.82	102.4033
4	110.848	118.39	119.64	116.2927
4.7	119.271	123.7	125.03	122.667
6	129.95	128.156	129.588	129.2313
7	134.94	128.38	129.822	131.0473
8	137.74	126.74	128.167	130.8823
9	138.98	123.91	125.3	129.3967

Table 5: Penetration depth in this study (in micrometer)

For each reticulographs penetration depth increases continuously with increasing incident angle and reaches a maximum. Fig. 30 shows the variation of penetration depth with respect to tilt angle of (0 2 -6) reflection in the crystal. Intuitively, penetration depth should increase as the tilt is increased, but this is not the case as it can be seen from Fig. 13. The reason being, we are tracking the same reflection as the crystal is tilted, by further tilting the sample Bragg's angle increases which implies longer wavelength is required to satisfy the Bragg's law $\lambda = 2d \sin \theta$. Longer wavelength (lower the X-ray energy) have higher mass absorption coefficient which results in lower penetration depth at higher tilt angle.
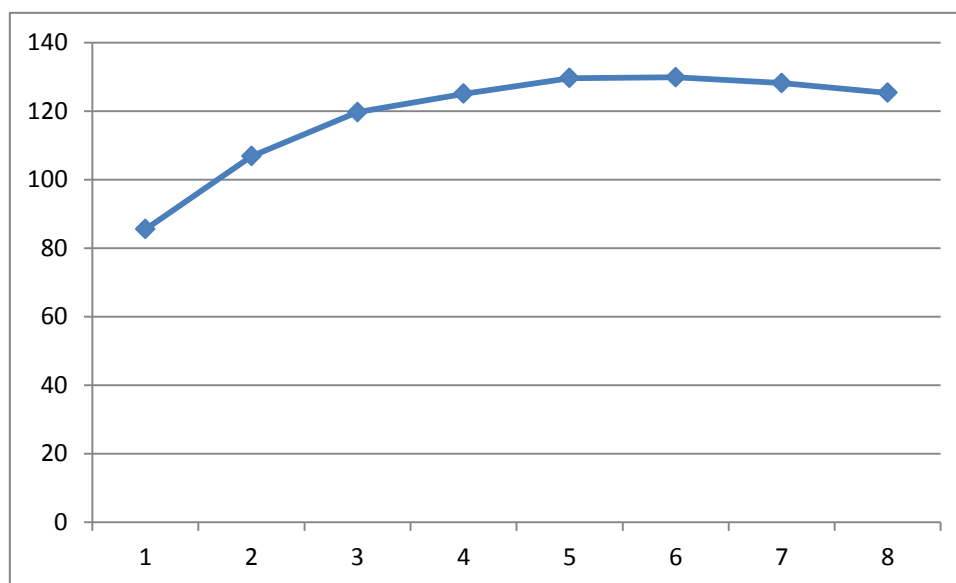
Figure 30: variation of penetration depth with respect to tilt angle of (02-6) reflection in the crystal; x-axis means the tile angle, y axis means the penetration depth.

3.5 Accurate Positioning Calculation of Films and Sample

Theoretically, the experiments should be conducted with $b=0$ degree (y-axis rotation angle) and $c=0$ degree (z-axis rotation angle); and the distance between lead and film (*sfd*) should be measured carefully in micrometer. But actually, these conditions are impossible to achieve during the experiment process. It is hard to get a diffraction pattern with perfect symmetry; and the length measuring tool in this study is a ruler in millimeter. These factors are critically important to the stress calculation process, especially the value of *sfd*, which I will talk about in the error analysis part. Therefore, accurate positioning of films and the sample is necessary.

In general, there are two ways to get the value of *b, c* and *sfd*. The first method is to compare the diffraction pattern from films with the one from LauePattern. This method could roughly tell the information of *b, c* and *sfd*, but it is time-consuming and of low accuracy. The second method, which is based on the relation of the distance between two reticulographic images, is highly accurate and scientific.

We know that for two diffraction spots, which are symmetrical about y-axis in this study, their distance in x-axis is in direct proportion to *sfd* if $b=0$ and $c=0$; and they are of the same height. Due to the influence of b and c, the two originally symmetrical diffraction spots' locations get changed and there will be discrepancy in both x-coordinates and y-coordinates. The discrepancy could reveal the information of *sfd*, *b* and *c*. Here, we select (-2 0 -6), (0 2 -6), (-4 0 -8) and (0 4 -8) diffractions for positioning process.
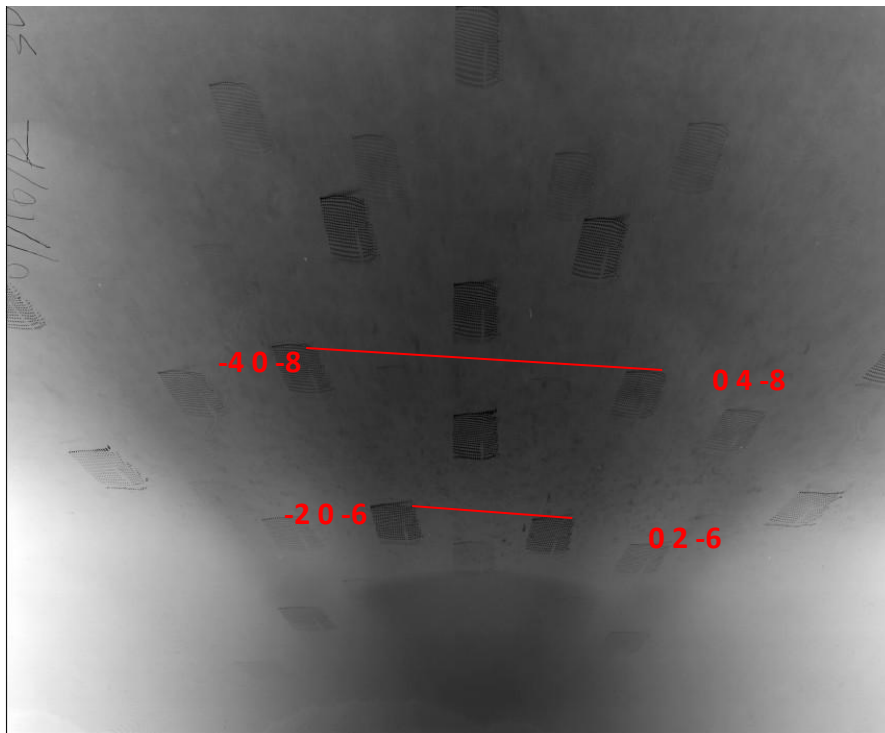
Figure 31: Four selected diffractions (*a*=2 degree)

For (-2 0 -6) and (0 2 -6), their plane normals could be written as:

$\bar{n}_{-20-6}(x, y, z)$

$$= \begin{bmatrix} \cos c & -\sin c & 0 \\ \sin c & \cos c & 0 \\ 0 & 0 & 1 \end{bmatrix} \cdot \begin{bmatrix} \cos b & 0 & \sin b \\ 0 & 1 & 0 \\ -\sin b & 0 & \cos b \end{bmatrix} \cdot \begin{bmatrix} 1 & 0 & 0 \\ 0 & \cos a & \sin a \\ 0 & -\sin a & \cos a \end{bmatrix} \cdot \begin{bmatrix} -2\wedge 0.5 \\ 6 \\ -2\wedge 0.5 \end{bmatrix}$$

$\bar{n}_{02-6}(x, y, z)$

$$= \begin{bmatrix} \cos c & -\sin c & 0 \\ \sin c & \cos c & 0 \\ 0 & 0 & 1 \end{bmatrix} \cdot \begin{bmatrix} \cos b & 0 & \sin b \\ 0 & 1 & 0 \\ -\sin b & 0 & \cos b \end{bmatrix} \cdot \begin{bmatrix} 1 & 0 & 0 \\ 0 & \cos a & \sin a \\ 0 & -\sin a & \cos a \end{bmatrix} \cdot \begin{bmatrix} 2\wedge 0.5 \\ 6 \\ -2\wedge 0.5 \end{bmatrix}$$

Using the equation $\vec{s_0} \times \vec{n} = -\vec{n} \times \vec{s}$, where $\vec{s_0} = [0,0,1]$, the vector of diffracted beam $\vec{s}$ could be calculated. We know that the two diffraction spots on the film have the same Z coordinate. Assume the (-2 0 -6) diffraction coordinate is (*m1, n1, z0*), (0 2 -6) is (*m2, n2, z0*).

$$n1 - n2 = s_{y1}\frac{z0}{s_{z1}} - s_{y2}\frac{z0}{s_{z2}};$$

$$m1 - m2 = s_{x1}\frac{z0}{s_{z1}} - s_{x2}\frac{z0}{s_{z2}};$$

where z0 has the same value as *sfd*, which is also undetermined.

In the above two equations, the value of *m1, m2, n1* and *n2* could be recorded from the film; s_{x1}, s_{x2}, s_{y1}, s_{y2}, s_{z1} and s_{z2} could be written as a function of *sfd*, *a* and *b*.

If the first equation divides the second one, we can get:

$$\frac{n1 - n2}{m1 - m2} = \frac{s_{z2} * s_{y1} - s_{z1} * s_{y2}}{s_{z2} * s_{x1} - s_{z1} * s_{x2}};$$

There are two undetermined factors in the above equation, *b* and *c*. Therefore, another equation with these two undetermined factors is necessary to solve the equations. The same processes are applied for (-4 0 -8) and (0 4 -8). Another equation is illustrated below:

$$\frac{n3 - n4}{m3 - m4} = \frac{s_{z4} * s_{y3} - s_{z3} * s_{y4}}{s_{z4} * s_{x3} - s_{z3} * s_{x4}};$$

With the above two equations, the value of *b* and *c* could be get. All calculation work is done by Mathematica. The code is shown below:

$$A = \begin{bmatrix} \cos c & -\sin c & 0 \\ \sin c & \cos c & 0 \\ 0 & 0 & 1 \end{bmatrix} \cdot \begin{bmatrix} \cos b & 0 & \sin b \\ 0 & 1 & 0 \\ -\sin b & 0 & \cos b \end{bmatrix} \cdot \begin{bmatrix} 1 & 0 & 0 \\ 0 & \cos a & \sin a \\ 0 & -\sin a & \cos a \end{bmatrix}$$

```
n1=A.{-2^0.5,6,-2^0.5}; n2=A.{2^0.5,6,-2^0.5};
x1=-2*n1[[1]]*n1[[3]];
y1=-2*n1[[2]]*n1[[3]];
z1=1-2*n1[[3]]^2;
x2=-2*n2[[1]]*n2[[3]];
```

y2=-2*n2[[2]]*n2[[3]];
z2=1-2*n2[[3]]^2;
n3=A.{-2^0.5,4,-2^0.5}; n4=A.{2^0.5,4,-2^0.5};
x3=-2*n3[[1]]*n3[[3]];
y3=-2*n3[[2]]*n3[[3]];
z3=1-2*n3[[3]]^2;
x4=-2*n4[[1]]*n4[[3]];
y4=-2*n4[[2]]*n4[[3]];
z4=1-2*n4[[3]]^2;
a=2 Degree;
NSolve[{(z2*y1-z1*y2)/(z2*x1-z1*x2)==-1/10,(z4*y3-z3*y4)/(z4*x3-z3*x4)==-11/100},
{b,c}]

As *b* and *c* are determined, the *sfd* could be calculated by:

$$sfd = \frac{s_{z1}s_{z2}(n1 - n2)}{s_{y1}s_{z2} - s_{y2}s_{z1}}$$

When the value of a, b,c and sfd are determined, the coordinate of each diffraction spot could be get from LauePattern. Here, we assume that the σ_{xx} in the fifth area equals zero to correct the coordinate of other points. The length of a unit cell in the grid is about 48 pixels for a stress free sample, which is almost the same as the length of the fifth square on the film; and the discrepancy in length is directly associated with σ_{xx}.Therefore, we use this assumption to locate the film.

3.6 Result and Discussion

To roughly calculate stress distribution, the sample was divided into nine areas. Each area is measured individually. Generally, the displacement information is recorded from the center of each area. In formation from highly distorted area is avoided.

(a)   **(b)**
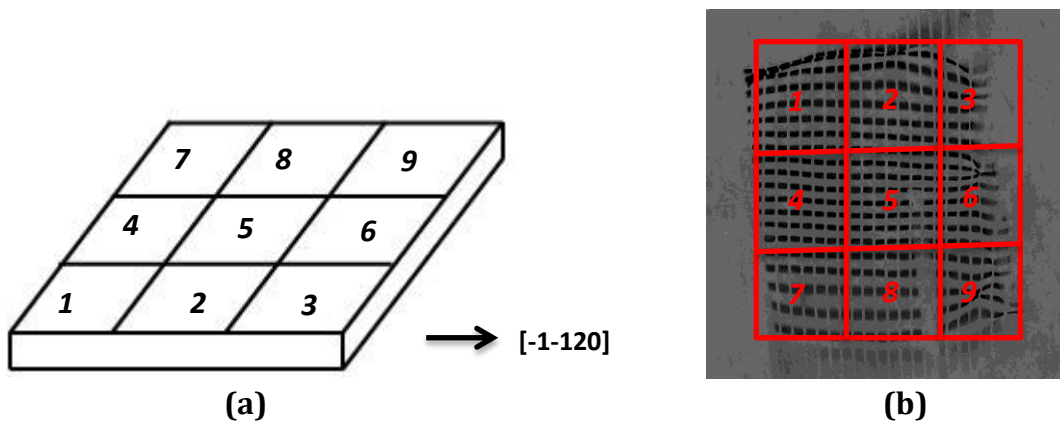
Figure 32: 9 areas on the sample (a) and reticulographic images (b)

Direct calculation result from SMART technique is a weighted average value and it is of

little use. Weighted average stress value at depth of 122μm is illustrated in the following table:

	1	2	3	4	5	6	7	8	9
xx	-2.763	-2.819	-2.635	-6.544	-6.382	-6.380	-1.233	-1.044	-0.878
yy	-1.842	-2.121	-1.923	-2.046	-2.033	-1.866	-0.066	0.153	0.139
zz	-4.195	-4.711	-4.388	-5.715	-5.636	-5.355	-0.580	-0.201	-0.239
xy	-1.133	-1.170	-1.210	-1.070	-0.971	-0.895	-0.593	-0.738	-0.873
xz	-5.602	-5.782	-5.978	-5.172	-4.695	-4.322	-2.796	-3.494	-4.140
yz	-1.040	-1.257	-1.128	-0.494	-0.512	-0.380	0.153	0.293	0.249

Table 6: weighted average stress value at depth on 122μm

Note that x, y and z here is the same as Fig. 8 in the experiment part. In order to calculate stress depth profile at an arbitrary location, we first plot calculated weighted average stress versus penetration depth and generate a best fit curve. This weighted average stress function is then transformed in order to reduce the equation into standard Laplace transform. Inverse Laplace Transform of this function will give the stress as a function of depth (z).

The mathematical transformation of weighted average stress into real space stress is pretty difficult. In Vish's study, he assumes the function of stress distribution in Laplace space as:

$$\bar{\sigma}(\tau) = \frac{a}{\tau} + b + c\tau + d\tau^2 + e\tau^3 + f\tau^4$$

where the value of *a, b, c, d, e* and *f* could be calculated if enough information is provided.

Another restrictive condition has to be applied here to control the function tendency, that is, $\bar{\sigma}(0) = 0$. Otherwise, the real space stress value may be magnified 100 times of the one in Laplace space after Inverse Laplace transformation. This assumption is not reasonable.

Therefore, in this study, the evaluation of the stress depth distribution $\bar{\sigma}(\tau)$ and $\sigma(z)$ is performed by fitting the experimental data by means of an exponentially damped polynom as successfully used by I. A. Denks and Hauk[27,28]. The functions are shown below:

$$\bar{\sigma}(\tau) = \frac{1}{\tau} \sum_{n=0}^{N} a_n \frac{n!}{(a_{N+1} + \frac{1}{\tau})^{n+1}}$$

$$\sigma(Z) = [\sum_{n=0}^{N} a_n Z^n] e^{-a_{N+1} Z}$$

Take σ_{xx} as an example; in area 1, experimentally determined weighted average stresses at various penetration depths are given in the table below. We only choose experimental data with few scattering here to minimize errors:

Penetration depth (μm)	80.80253	102.4033	116.2927	122.667	129.2313
Average stress (GPa)	-2.22	-2.88	-2.86	-3.00	-3.00

Table 7: Average stress value at area #1 (σ_{xx})

Using the equation above, the stress in Laplace space is:

$$\bar{\sigma}(\tau) = \frac{1}{\tau}\left[\frac{1.08}{-0.0075 + \frac{1}{\tau}} + \frac{0.0011}{\left(-0.0075 + \frac{1}{\tau}\right)^2} + \frac{-3.504 * 10^{-7}}{\left(-0.0075 + \frac{1}{\tau}\right)^3}\right]$$

The fitting diagram is:
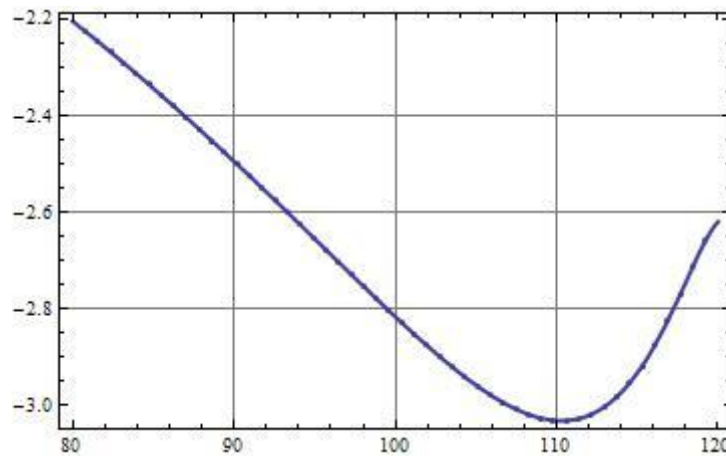
Figure 33: Fitting diagram of σ_{xx}, $\tau \in (80,120)$

The inverse Laplace transformation is achieved by the following codes:

```
curve1=(1/s)*(y[x]/.x->1/s);
curve1;
sigmaxx=InverseLaplaceTransform[curve1,s,t]
Plot[y[x],{x,80,120},Mesh->True,AxesLabel->{depth,stress},PlotStyle->Thick,GridLine
s->Automatic,Frame->True]
Plot[sigmaxx,{t,80,120},Mesh->True,AxesLabel->{depth,stress},PlotStyle->Thick,Grid
Lines->Automatic,Frame->True]
```

Using Mathematica, the inverse Laplace transformation could be easily calculated as:

$$\sigma(Z) = -1.0801e^{0.007545*Z} + 0.001101e^{0.007545*Z} * Z - 1.7523e^{0.007545*Z} * Z^2$$

where Z is the depth from surface.

Thus the function curve is:
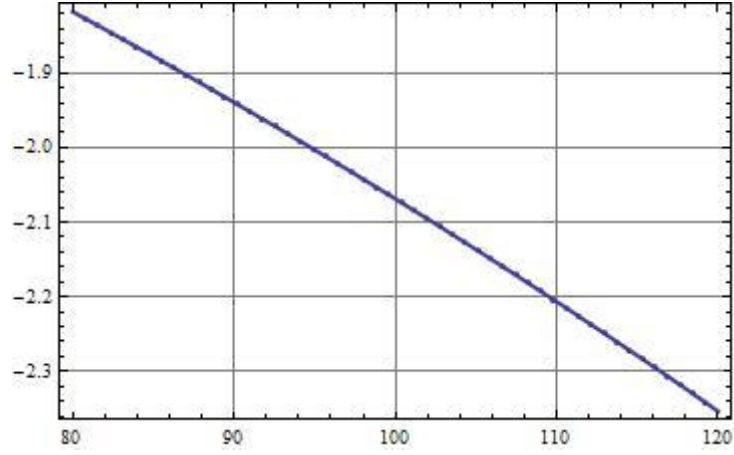
Figure 34: Real space σ_{xx} stress in area #1, $Z \in (80,120)$

The real space stress value in area #1 with depth from 80 to 120 micrometers is shown in the following table:

Depth (μm)	σ_{xx} in real space (GPa)
80	−1.81
90	−1.93
100	−2.06
110	−2.2
120	−2.35

Table 8: σ_{xx} values in real space, with depth of 80, 90, 100, 110 and 120μm

We have repeated this calculation over the crystal area in order to determine the full state of stress determined at each point within the crystal. Using the stress depth profiles we have generated stress maps at a depth below the surface, such as 80, 90, 100, 110 and 120μm. They are shown in the following:

	1	2	3	4	5	6	7	8	9
σ_{xx}	−1.81	−1.71	−1.28	−0.35	0	0.2	−0.52	−1.08	−0.45
σ_{yy}	−2.79	−2.91	−2.55	−2.24	−2.1	−1.97	−0.34	−0.34	−0.31
σ_{zz}	−4.92	−4.82	−4.42	−2.77	−2.42	−2.19	−1.86	−1.46	−1.24
σ_{xy}	−0.54	−0.56	−0.59	−0.42	−0.46	−0.54	−0.33	−0.37	−0.36
σ_{xz}	−3.58	−3.72	−3.98	−2.68	−3.03	−3.62	−2.18	−2.49	−2.45
σ_{yz}	−1.66	−1.63	−1.57	−1.16	−1.1	−1.05	−0.15	−0.1	−0.06

Table 9: Real space stress at 9 areas in the crystal in depth of 80μm, GPa

	1	2	3	4	5	6	7	8	9
σ_{xx}	−1.93	−1.83	−1.38	−0.37	0	0.21	−0.62	−1.29	−0.63
σ_{yy}	−2.94	−3.04	−2.69	−2.38	−2.23	−2.1	−0.38	−0.38	−0.35
σ_{zz}	−5.2	−5.1	−4.68	−2.92	−2.55	−2.31	−1.99	−1.58	−1.35
σ_{xy}	−0.57	−0.58	−0.62	−0.44	−0.48	−0.57	−0.34	−0.39	−0.38
σ_{xz}	−3.79	−3.93	−4.21	−2.83	−3.21	−3.83	−2.31	−2.64	−2.59
σ_{yz}	−1.74	−1.71	−1.65	−1.21	−1.16	−1.1	−0.17	−0.11	−0.07

Table 10: Real space stress at 9 areas in the crystal in depth of 90μm, GPa

	1	2	3	4	5	6	7	8	9
σ_{xx}	−2.06	−1.95	−1.48	−0.39	0	0.22	−0.73	−1.52	−0.83
σ_{yy}	−3.09	−3.17	−2.84	−2.52	−2.37	−2.24	−0.42	−0.42	−0.39
σ_{zz}	−5.5	−5.39	−4.95	−3.08	−2.69	−2.43	−2.13	−1.7	−1.46
σ_{xy}	−0.59	−0.61	−0.65	−0.46	−0.51	−0.6	−0.36	−0.41	−0.40
σ_{xz}	−4	−4.14	−4.44	−2.98	−3.39	−4.05	−2.45	−2.79	−2.74
σ_{yz}	−1.83	−1.79	−1.73	−1.27	−1.21	−1.15	−0.18	−0.12	−0.08

Table 11: Real space stress at 9 areas in the crystal in depth of 100μm, GPa

	1	2	3	4	5	6	7	8	9
σ_{xx}	−2.2	−2.09	−1.59	−0.41	0	0.23	−0.85	−1.77	−1.05
σ_{yy}	−3.26	−3.31	−3.00	−2.67	−2.52	−2.39	−0.48	−0.47	−0.43
σ_{zz}	−5.82	−5.7	−5.24	−3.24	−2.83	−2.57	−2.28	−1.83	−1.59
σ_{xy}	−0.62	−0.64	−0.68	−0.48	−0.53	−0.62	−0.38	−0.43	−0.42
σ_{xz}	−4.22	−4.36	−4.69	−3.14	−3.59	−4.28	−2.6	−2.95	−2.9
σ_{yz}	−1.91	−1.88	−1.81	−1.33	−1.27	−1.2	−0.2	−0.13	−0.09

Table 12: Real space stress at 9 areas in the crystal in depth of 110μm, GPa

	1	2	3	4	5	6	7	8	9
σ_{xx}	−2.35	−2.23	−1.7	−0.43	0	0.24	−0.98	−2.04	−1.28
σ_{yy}	−3.43	−3.46	−3.16	−2.83	−2.68	−2.55	−0.53	−0.52	−0.48
σ_{zz}	−6.15	−6.03	−5.54	−3.41	−2.98	−2.7	−2.44	−1.98	−1.72
σ_{xy}	−0.65	−0.67	−0.71	−0.5	−0.56	−0.65	−0.4	−0.45	−0.44
σ_{xz}	−4.46	−4.6	−4.95	−3.31	−3.79	−4.52	−2.76	−3.13	−3.06
σ_{yz}	−2.01	−1.97	−1.9	−1.38	−1.33	−1.26	−0.22	−0.14	−0.10

Table 13: Real space stress at 9 areas in the crystal in depth of 120μm, GPa

Note that area1~9 in the above tables correspond with Figure 32(b).

Theoretically, this technique could be applied to predict stress distribution in any depth inside the crystal by extrapolating the curve, in the condition that enough experimental data is collected. The surface stress distribution of the sample is shown in the following, which is measured by Raman spectroscopy. Its principle is shown in Appendix III.
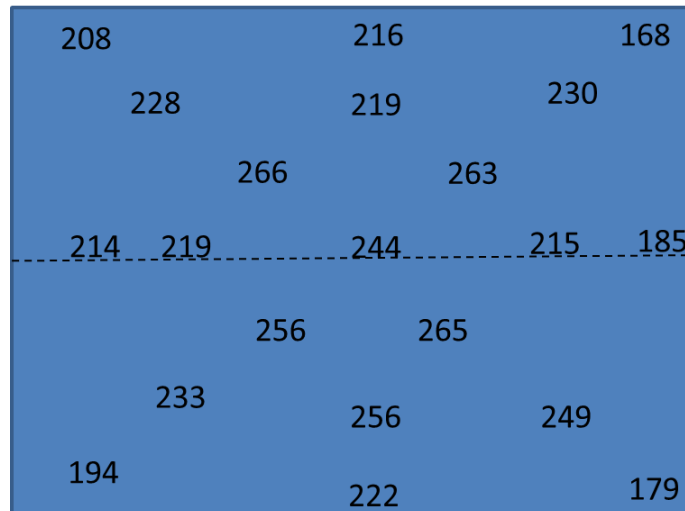
Figure 35: Surface stress values measured by Raman spectroscopy (MPa)

Actually, the stress distribution from Raman spectroscopy is not the same as the result if we extrapolate the curve to z=0. It does not mean that the technique of SMART is unreasonable. From figure 34, we can find that the real space stress value is almost linear to depth between 80 and 120μm. If we extrapolate the curve, the assumption that this tendency will continue to the surface area has to be made. In fact, the gradient changes a lot for the near-surface regions, which is illustrated in figure 36:
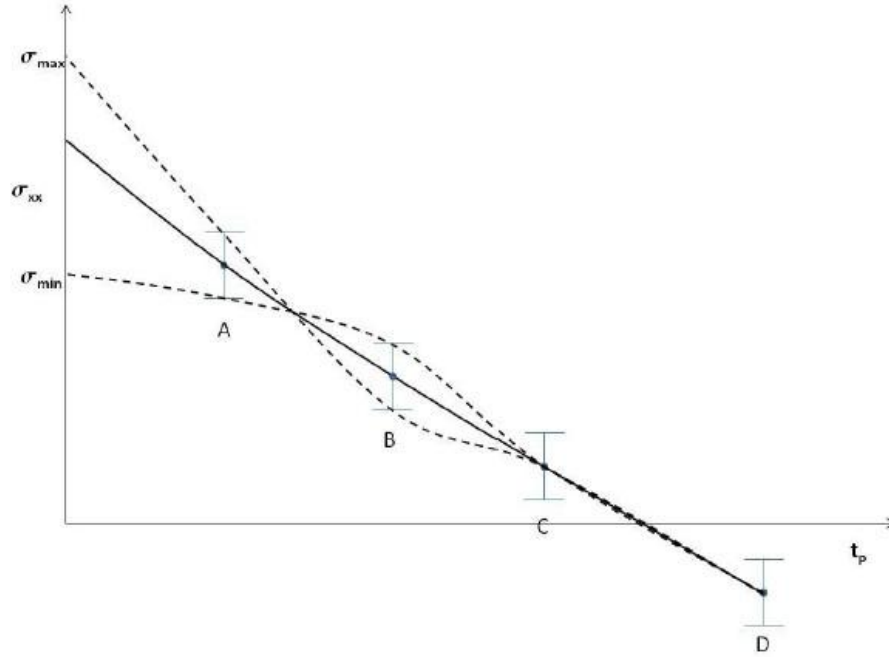
Figure 36: Schematic plot of depth profile showing error associated in determining surface stress.[20]

Assume the stress distribution in this study is between C and D in figure 36. It shows that the curve may changes a lot for depth from 0 to 80µm. Therefore, the discrepancy may exist if we simply extrapolate the curve.

3.7 Error Analysis

There are two kinds of errors exist in the experimental measurement: random error and system error. Random errors could be minimized while system errors cannot. The concept of precision is related to random error. Minimizing the random error in measurement increases the precision of the result whereby increasing the repeatability and reproducibility. The concept of accuracy is related to systematic error. Systematic error is the bias in the experimental system which pushes the results in the same direction. Both errors will be discussed here.

The first error, which is also one main error in depth profiling, arises from the way we select three diffraction spot. In this technique, the vector of diffracted beam is defined as:

$$\vec{s} = A(x_1, y_1, z_1) - B(x_2, y_2, z_2)$$

where $A(x_1, y_1, z_1)$ is the coordinate of one certain point on the film, $B(x_2, y_2, z_2)$ is the coordinate of the correspondent point on the grid.

The origin of diffracted beam is set on the grid instead of sample for its measurability.

As mentioned before, we have to select 3 different diffraction spots to solve the equation. However, the grazing geometry restricts that there has to be a distance between sample and grid to allow the incident beam covering the sample, which is shown in the following figure. Due to this restriction, the stress values we get from three different diffraction spots do not reflect stress distribution of that certain point on the sample. The discrepancy increases as the distance increases. To minimize this error, we have to select diffraction spots that are closest to the center axis.
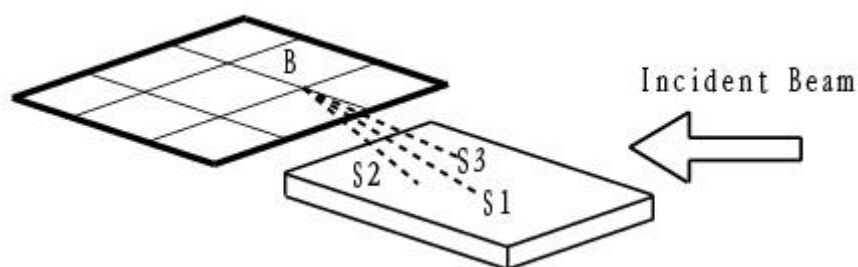
Figure 37: Schematic of errors from the grazing geometry restriction

Also, the process of taking average value of penetration depth of three diffraction spots can cause errors by influencing fitting functions. Take stresses in area #1 as an example. As shown in the former part, if we take the average penetration depth in the calculation, real space stress distribution and stress-depth function curve are shown in Figure 34 and Table 8. Repeat the calculation for the circumstance that penetration depth is set the same as (-2 2 -8). The results are shown in below:

Depth	xx	yy	zz	xy	xz	yz
80	−2.00	−3.01	−6.51	−0.6	−3.29	−1.92
90	−2.14	−3.16	−6.82	−0.66	−3.68	−2.01

Table 14: Stress distribution with depth of 80 and 90μm if penetration depth is set the same as (-2 2 -8) reflection

Stress values when penetration depth is set as the average are:

Depth	xx	yy	zz	xy	xz	yz
80	−1.81	−2.79	−4.92	−0.54	−3.58	−1.66
90	−1.93	−2.94	−5.2	−0.57	−3.79	−1.74

Table 15: Stress distribution with depth of 80 and 90μm if penetration depth is set as the average

From the above two tables, we find that the definition of penetration depth has strong influence to the real space stress value. Each 1μm will cause changes of 15MPa in *xx* stress, 27MPa in *yy* stress, 200MPa in *zz* stress, 7MPa in *xy* stress, 30MPa in *xz* stress and 30MPa in yz stress. Anyway, the tendency of the real space stress function will not change with penetration depth.

Errors come from the uncertainty of film position and film distance is corrected in the former part. Another error in this study is due to the shape change of the sample. Assume a rectangular shaped crystal before packaging. After processing at higher temperature and subsequent cooling of the package leads to bending of the packaged assembly (shown on Fig. 36). As a result of this bending in-plane normal stress are maximum at the top (tensile) and minimum (compressive) at the bottom. Shape of the crystal itself does not play a role in stress determination using SMART technique. However, bending of crystallographic plane will occur if the crystal changes shape due to bending. The bending of crystallographic planes is incorporated in the smart technique and no special consideration is required for change in shape.

(A) (B)
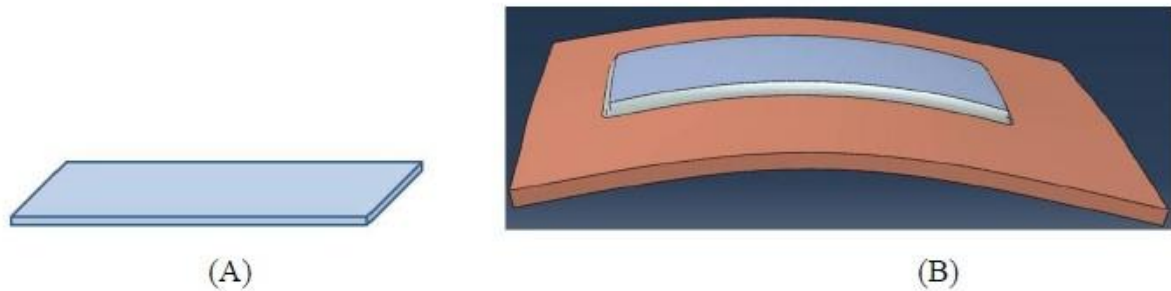
Figure 38: Schematic of a silicon die (A) before packing (B) after packing[21]

3.8 Conclusion

A novel non-destructive technique based on ray tracing and x-ray reticulography to determine all six stress components is discussed in detail in this study. Residue strain is calculated by the equation $\vec{n} = \vec{n_0} - \nabla(\vec{n_0} \cdot \vec{u})$. Stress directly derived from strains represents the stress values in Laplace space. Inverse Laplace transformation has to be applied to get the real space stress information, which is of much more importance. This calculation is repeated for each array points on the crystal surface defined by the grid and complete stress profile is generated for the crystal up to penetration depth. Error origins are evaluated. Stress distribution measured by Raman spectroscopy is listed here.

3.9 Future Work

To get better results, the experiment could get improvements in the following aspects: (a) get rid of the assumption that σ_{xx} in the fifth area equals zero; this assumption could influence the absolute stress values but will not have effects on the curve tendency; (b) 3 different diffraction spots have to be selected to solve the equations and this process will cause discrepancy in penetration depth calculation; its influence has been discussed in the error analysis part; this kind of error is unavoidable in this model, which means, better models have to be introduced here.

References

[1] M.V. Laue, Ann Phys., **26**: pp. 55-68 (1936)

[2] D. K. Bowen and B. K. Tanner, in "*High Resolution X-Ray Diffractometry and Topography*", Taylor & Francis, pp. 225 (1998)

[3] Vish Sarkar, *Defect characterization and stress analysis by white beam synchrotron X-ray topography in single crystal semiconducting materials,* pp.127

[4] Vish Sarkar, *Defect characterization and stress analysis by white beam synchrotron X-ray topography in single crystal semiconducting materials,* pp.136

[5] D.C. Reynolds, D.C. Look, B. Jogai, Solid State Commun., **99**: pp.873-875 (1996)

[6] P. Zu, Z.K. Tang, G.K.L. Wong, M. Kawasaki, A. Ohtomo,H. Koinuma, Y. Segawa, Solid State Commun., **103**, pp.459-463 (1997)

[7] http://en.wikipedia.org/wiki/Wurtzite_crystal_structure

[8] Nathan Johann Nicholas, et al., *The Mechanism for Hydrothermal growth of zinc oxide,* CrystEngComm, 2012, **14**, 1232

[9] J.P. Hirth and J. Lothe, "*Theory of Dislocations*", 2nd Edition, John Wiley& Sons, pp.60 (1982)

[10] J.P. Hirth and J. Lothe, "*Theory of Dislocations*", 2nd Edition, John Wiley& Sons, pp.78 (1982)

[11] E. H. Yoffe, Phil. Mag. **6**, 1147 (1961)

[12] J. D. Eshelby and A. N. Stroh, Phil. Mag. **42,** 1401 (1951)

[13] F.Z. Wu, S.Byrappa, H.H. Wang, Y.Chen, B. Raghothamachar, M. Dudley, E.K. Sanchez, G. Chung, D. Hansen, S.G. Mueller and M.J. Loboda, Mater. Res. Soc. Symp. Proc. **1433** (2012).

[14] X. R. Huang, M. Dudley, W. M. Vetter, W. Huang, W. Si, and C. H. Carter, Jr., J. Appl. Cryst. **32**, 516 (1999)

[15] D. I. Ma, et al., *Characterization of the Electrical Bias Induced Strain Variation in Metal-Oxide Semiconductor Field-Effect Transistors Using X-Ray Double Crystal Topography.* Journal of Vacuum Science & Technology a-Vacuum Surfaces and Films, **10**(4): p. 1012-1019 (1992)

[16] M. Ranjan, et al., *Die cracking in flip chip assemblies.* Proc. - Electron. Compon. Technol. Conf., **48th**: p. 729-733 (1998)

[17] Fujii, N., K. Inui, and S. Kozaki, *X-ray stress measurement of mounted silicon chips*. Jpn. J. Appl. Phys., Part 1, 1997. **36**(12A): p. 7411-7414.

[18] Kikuta, S., K. Kohra, and Y. Sugita, *Measurements on Local Variations in Spacing and Orientation of Lattice Plane of Silicon Single Crystals by X-Ray Double-Crystal Topography.* Japanese Journal of Applied Physics, 1966. **5**(11): p. 1047

[19] McNally, P.J., et al., *Mapping of mechanical, thermomechanical and wire-bond strain fields in packaged Si integrated circuits using synchrotron white beam x-ray topography.* Ieee Transactions on Components and Packaging Technologies, 2001. **24**(1): p. 76-83

[20] Vish Sarkar, *Defect characterization and stress analysis by white beam synchrotron X-ray topography in single crystal semiconducting* materials, pp.26-64

[21] Vish Sarkar, *Defect characterization and stress analysis by white beam synchrotron X-ray topography in single crystal semiconducting* materials, pp.65-89

[22] I.C. Noyan and J.B. Cohen, *Residual stress : measurement by diffraction and*

interpretation. Materials research and engineering. New York: Springer-Verlag. x, 276 p. (1987)

[23] T. Manns, A. Rothkirch, and B. Scholtes, *Residual stress determination in surface treated alumina samples applying beam limiting masks.* Powder Diffraction, **24**(2): p. S77-S81 (2009).

[24] C. Genzel , *Evaluation of stress gradients sigma(ij)(z) from their discrete laplace transforms sigma(ij)(tau(k)) obtained by X-ray diffraction performed in the scattered vector mode.* Physica Status Solidi a-Applied Research, **156**(2): p. 353-363 (1996).

[25] Vish Sarkar, *Defect characterization and stress analysis by white beam synchrotron X-ray topography in single crystal semiconducting* materials, pp.128

[26] X. R. Huang, "*LauePt, a graphical-user-interface program for simulating and analyzing white- beam X-ray diffraction Laue patterns*", Journal of Applied Crystallography, Vol. 43, 926-928 (2010)

[27] I. A. Denks, et al., *An Experimental Approach to the Problem of Transforming Stress Distributions from Laplace into Real Space*, Zeitschrift Fur Kristallographie, p. 69-74 (2009)

[28] Hauk, V. & Krug, K., HTM, **39**, 273 (1984)

Appendix I. Codes for Threading Dislocations

Codes for Threading Edge Dislocation

$\{b, t, d, \alpha, \Theta, \Theta0, \text{magnification}, v\}$
$$= \{0.0003624, 500, 170000, 10.608\text{Degree}, 0\text{Degree}, 0\text{Degree}, 10, 0.351\};$$

$\text{rx} = -\text{Cos}[2\text{Degree}];$

$\text{ry} = 0;$

$\text{rz} = -\text{Sin}[2\text{Degree}];$

$\text{nx0} = \text{Cos}[51.3044\text{Degree}];$

$\text{ny0} = 0;$

$\text{nz0} = \text{Sin}[51.3044\text{Degree}];$

$$\text{uxTED} = \frac{1}{8\pi(-1+v)(x0^2+y0^2)} b(-2x0y0\text{Cos}[\Theta] + 4(-1+v)(x0^2$$
$$+ y0^2)\text{ArcTan}[\frac{y0\text{Cos}[\Theta] - x0\text{Sin}[\Theta]}{x0\text{Cos}[\Theta] + y0\text{Sin}[\Theta]}]\text{Cos}[\Theta] + (x0^2 - y0^2 + (-1$$
$$+ 2v)(x0^2 + y0^2)\text{Log}[x0^2 + y0^2])\text{Sin}[\Theta]);$$

$$\text{uyTED} = \frac{1}{8\pi(-1+v)(x0^2+y0^2)} b(\text{Cos}[\Theta](x0^2 - y0^2 - (-1+2v)(x0^2+y0^2)\text{Log}[x0^2$$
$$+ y0^2]) + 2x0y0\text{Sin}[\Theta] + 4(-1+v)(x0^2$$
$$+ y0^2)\text{ArcTan}[\frac{y0\text{Cos}[\Theta] - x0\text{Sin}[\Theta]}{x0\text{Cos}[\Theta] + y0\text{Sin}[\Theta]}]\text{Sin}[\Theta]);$$

$\text{ux}[x0\_, y0\_, z0\_] = \text{uxTED}; \text{uy}[x0\_, y0\_, z0\_] = \text{uyTED}; \text{uxDx} = D[\text{ux}[x0, y0, z0], x0]; \text{uxDy}$
$\qquad = D[\text{ux}[x0, y0, z0], y0]; \text{uxDz} = D[\text{ux}[x0, y0, z0], z0]; \text{uyDx}$
$\qquad = D[\text{uy}[x0, y0, z0], x0]; \text{uyDy} = D[\text{uy}[x0, y0, z0], y0]; \text{uyDz}$
$\qquad = D[\text{uy}[x0, y0, z0], z0]; \text{uzDx} = 0; \text{uzDy} = 0; \text{uzDz} = 0;$

$\text{filmDensity} = \text{Table}[0, \{i, 1, 500\}, \{j, 1, 500\}];$

$\text{Do}[$

$\text{If}[x0 == 0 \&\& y0 == 0, \text{Continue}[\quad]];$

$z0 = x0 * \text{Tan}[\Theta0];$

$\text{nx} = \text{nx0} - \text{nx0} * \text{uxDx} - \text{ny0} * \text{uyDx} - \text{nz0} * \text{uzDx};$

$\text{ny} = \text{ny0} - \text{nx0} * \text{uxDy} - \text{ny0} * \text{uyDy} - \text{nz0} * \text{uzDy};$

$\text{nz} = \text{nz0} - \text{nx0} * \text{uxDz} - \text{ny0} * \text{uyDz} - \text{nz0} * \text{uzDz};$

$$\text{rx1} = \frac{-\text{nx}^2\text{rx} + \text{ny}^2\text{rx} + \text{nz}^2\text{rx} - 2\text{nxnyry} - 2\text{nxnzrz}}{\text{nx}^2 + \text{ny}^2 + \text{nz}^2};$$

$$ry1 = \frac{-2nxnyrx + nx^2ry - ny^2ry + nz^2ry - 2nynzrz}{nx^2 + ny^2 + nz^2};$$

$$rz1 = \frac{-2nxnzrx - 2nynzry + nx^2rz + ny^2rz - nz^2rz}{nx^2 + ny^2 + nz^2};$$

$$x1 = \frac{rz1x0 - rx1z0 + drx1Cos[\alpha] + drz1Sin[\alpha]}{rz1Cos[\alpha] - rx1Sin[\alpha]} * \text{magnification};$$

$$y1$$

$$= \frac{dry1 + rz1y0Cos[\alpha] - ry1z0Cos[\alpha] + ry1x0Sin[\alpha] - rx1y0Sin[\alpha]}{rz1Cos[\alpha] - rx1Sin[\alpha]}$$

$* \text{magnification};$

$m = \text{Floor}[x1]; n = \text{Floor}[y1];$

$\text{If}[m \geq -249\&\&m \leq 250\&\&n \geq -249\&\&n \leq 250, \text{filmDensity}[[m + 250, n + 250]]+$

$$= 1],$$

$\{x0, -25, 25, 0.035\},$
$\{y0, -25, 25, 0.035\}]$
$\text{ListDensityPlot}[\text{filmDensity}, \text{Mesh} \rightarrow \text{None}]$
$\text{ColorNegate}[\text{ListDensityPlot}[\text{filmDensity}, \text{Mesh} \rightarrow \text{None}, \text{ImageSize}$

Codes for Threading Screw Dislocation

$\{b, t, d, \alpha, \text{magnification}, \Theta0\}$
$= \{-0.00051948, 500, 150000, 10.6088\text{Degree}, 10, 0\text{Degree}\};$
$rx = -Cos[2\text{Degree}];$
$ry = 0;$
$rz = -Sin[2\text{Degree}];$
$nx0 = Cos[51.3044\text{Degree}];$
$ny0 = 0;$
$nz0 = Sin[51.3044\text{Degree}];$

$$u\Theta = \frac{-b}{2\text{Pi}} * \sum_{n=0}^{3} ((-1)^n$$

$$* \left(\frac{\sqrt{x0^2 + y0^2}}{(2n+1)t - (z0+t) + \sqrt{((2n+1)t - (z0+t))^2 + (x0^2 + y0^2)}} \right.$$

$$\left. - \frac{\sqrt{x0^2 + y0^2}}{(2n+1)t + (z0+t) + \sqrt{((2n+1)t + (z0+t))^2 + (x0^2 + y0^2)}} \right));$$

$$ux[x0\_, y0\_, z0\_] = u\Theta * \frac{-y0}{\sqrt{x0^2 + y0^2}};$$

$$uy[x0\_, y0\_, z0\_] = u\Theta * \frac{x0}{\sqrt{x0^2 + y0^2}};$$

$$uz[x0\_, y0\_, z0\_] = \frac{b}{2\text{Pi}} \text{ArcTan}[\frac{y0}{x0}];$$

$uxDx = D[ux[x0, y0, z0], x0];$

$uxDy = D[ux[x0, y0, z0], y0];$

$uxDz = D[ux[x0, y0, z0], z0];$

$uyDx = D[uy[x0, y0, z0], x0];$

$uyDy = D[uy[x0, y0, z0], y0];$

$uyDz = D[uy[x0, y0, z0], z0];$

$uzDx = D[uz[x0, y0, z0], x0];$

$uzDy = D[uz[x0, y0, z0], y0];$

$uzDz = 0;$

$\text{filmDensity} = \text{Table}[0, \{i, 1, 500\}, \{j, 1, 500\}];$

$\text{Do}[$

$\text{If}[x == 0 \&\& y == 0, \text{Continue}[]];$

$z0 = 0;$

$nx = nx0 - nx0 * uxDx - ny0 * uyDx - nz0 * uzDx;$

$ny = ny0 - nx0 * uxDy - ny0 * uyDy - nz0 * uzDy;$

$nz = nz0 - nx0 * uxDz - ny0 * uyDz - nz0 * uzDz;$

$$rx1 = \frac{-nx^2 rx + ny^2 rx + nz^2 rx - 2nxnyry - 2nxnzrz}{nx^2 + ny^2 + nz^2};$$

$$ry1 = \frac{-2nxnyrx + nx^2 ry - ny^2 ry + nz^2 ry - 2nynzrz}{nx^2 + ny^2 + nz^2};$$

$$rz1 = \frac{-2nxnzrx - 2nynzry + nx^2 rz + ny^2 rz - nz^2 rz}{nx^2 + ny^2 + nz^2};$$

$$x1 = \frac{rz1x0 - rx1z0 + drx1\cos[\alpha] + drz1\sin[\alpha]}{rz1\cos[\alpha] - rx1\sin[\alpha]} * \text{magnification};$$

$$y1 = \frac{dry1 + rz1y0\cos[\alpha] - ry1z0\cos[\alpha] + ry1x0\sin[\alpha] - rx1y0\sin[\alpha]}{rz1\cos[\alpha] - rx1\sin[\alpha]}$$

$$* \text{magnification};$$

$m = \text{Floor}[x1]; n = \text{Floor}[y1];$

$\text{If}[m \geq -249\&\&m \leq 250\&\&n \geq -249\&\&n \leq 250, \text{filmDensity}[[m + 250, n + 250]]+$

$$= 1],$$

$\{x0, -25, 25, 0.035\},$
$\{y0, -25, 25, 0.035\}]$
$\text{ListDensityPlot}[\text{filmDensity}, \text{Mesh} \rightarrow \text{None}]$
$\text{ColorNegate}[\text{ListDensityPlot}[\text{filmDensity}, \text{Mesh} \rightarrow \text{None}, \text{ImageSize}$

Codes for Mixed Dislocations

$\{b1, b2, t, d, \alpha, \Theta, \Theta0, \text{magnification}, \nu\}$
$= \{-0.0005, 0.0003426, 500, 170000, 10.608\text{Degree}, 0\text{Degree}, 0\text{Degree}, 10, 0.351\};$
$n1 = 1; n2 = 1;$
$rx = -\cos[2\text{Degree}];$
$ry = 0;$
$rz = -\sin[2\text{Degree}];$
$nx0 = \cos[51.3044\text{Degree}];$
$ny0 = 0;$
$nz0 = \sin[51.3044\text{Degree}];$
us

$$= \frac{-b1}{2\text{Pi}} \sum_{n=0}^{3} ((-1)\hat{}n(\frac{(x0\hat{}2 + y0\hat{}2)\hat{}0.5}{(2n + 1)t - (z0 + t) + \sqrt{((2n + 1)t - (z0 + t))\hat{}2 + (x0\hat{}2 + y0\hat{}2)}}$$

$$- \frac{(x0\hat{}2 + y0\hat{}2)\hat{}0.5}{(2n + 1)t + (z0 + t) + \sqrt{((2n + 1)t + (z0 + t))\hat{}2 + (x0\hat{}2 + y0\hat{}2)}}));$$

$$\text{uxs}[x0\_, y0\_, z0\_] = \frac{-y0}{\sqrt{x0^2 + y0^2}} * us;$$

$$uys[x0\_, y0\_, z0\_] = \frac{x0}{\sqrt{x0^2 + y0^2}} * us;$$

$$uzs[x0\_, y0\_, z0\_] = \frac{b1}{2Pi} * ArcTan[\frac{y0}{x0}];$$

$$uxT[x0\_, y0\_, z0\_] = \frac{b2}{2\pi} (ArcTan[\frac{y0}{x0}] + \frac{x0y0}{2(1 - v)(x0^\wedge 2 + y0^\wedge 2)});$$

$$uyT[x0\_, y0\_, z0\_]$$

$$= -\frac{b2}{2\pi} \left(\frac{1 - 2v}{4(1 - v)} Log[x0^2 + y0^2] + \frac{x0^2 - y0^2}{4(1 - v)(x0^2 + y0^2)} \right);$$

$$uxt[x0\_, y0\_, z0\_] = Cos[\Theta] * uxT[x0, y0, z0] - Sin[\Theta] * uyT[x0, y0, z0];$$
$$uyt[x0\_, y0\_, z0\_] = Cos[\Theta] * uyT[x0, y0, z0] + Sin[\Theta] * uxT[x0, y0, z0];$$
$$ux[x0\_, y0\_, z0\_] = n2 * uxt[x0, y0, z0] + n1 * uxs[x0, y0, z0];$$
$$uy[x0\_, y0\_, z0\_] = n2 * uyt[x0, y0, z0] + n1 * uys[x0, y0, z0];$$
$$uz[x0\_, y0\_, z0\_] = n1 * uzs[x0, y0, z0];$$
$$uxDx = D[ux[x0, y0, z0], x0];$$
$$uxDy = D[ux[x0, y0, z0], y0];$$
$$uxDz = D[ux[x0, y0, z0], z0];$$
$$uyDx = D[uy[x0, y0, z0], x0];$$
$$uyDy = D[uy[x0, y0, z0], y0];$$
$$uyDz = D[uy[x0, y0, z0], z0];$$
$$uzDx = D[uz[x0, y0, z0], x0];$$
$$uzDy = D[uz[x0, y0, z0], y0];$$
$$uzDz = 0;$$
$$filmDensity = Table[0, \{i, 1, 500\}, \{j, 1, 500\}];$$
Do[

$$If[x0 == 0 \&\& y0 == 0, Continue[\quad]];$$

$$z0 = x0 * Tan[\Theta 0];$$
$$nx = nx0 - nx0 * uxDx - ny0 * uyDx - nz0 * uzDx;$$
$$ny = ny0 - nx0 * uxDy - ny0 * uyDy - nz0 * uzDy;$$
$$nz = nz0 - nx0 * uxDz - ny0 * uyDz - nz0 * uzDz;$$

$$rx1 = \frac{-nx^2 rx + ny^2 rx + nz^2 rx - 2nxnyry - 2nxnzrz}{nx^2 + ny^2 + nz^2};$$

$$ry1 = \frac{-2nxnyrx + nx^2 ry - ny^2 ry + nz^2 ry - 2nynzrz}{nx^2 + ny^2 + nz^2};$$

$$rz1 = \frac{-2nxnzrx - 2nynzry + nx^2 rz + ny^2 rz - nz^2 rz}{nx^2 + ny^2 + nz^2};$$

$$x1 = \frac{rz1x0 - rx1z0 + drx1\text{Cos}[\alpha] + drz1\text{Sin}[\alpha]}{rz1\text{Cos}[\alpha] - rx1\text{Sin}[\alpha]} * \text{magnification};$$

y1

$$= \frac{dry1 + rz1y0\text{Cos}[\alpha] - ry1z0\text{Cos}[\alpha] + ry1x0\text{Sin}[\alpha] - rx1y0\text{Sin}[\alpha]}{rz1\text{Cos}[\alpha] - rx1\text{Sin}[\alpha]}$$

$* \text{magnification};$

$m = \text{Floor}[x1]; n = \text{Floor}[y1];$

$\text{If}[m \geq -249 \&\& m \leq 250 \&\& n \geq -249 \&\& n \leq 250, \text{filmDensity}[[m + 250, n + 250]]+$

$= 1],$

$\{x0, -25, 25, 0.035\},$
$\{y0, -25, 25, 0.035\}]$
$\text{ListDensityPlot}[\text{filmDensity}, \text{Mesh} \rightarrow \text{None}]$
$\text{ColorNegate}[\text{ListDensityPlot}[\text{filmDensity}, \text{Mesh} \rightarrow \text{None}, \text{ImageSize}$

Appendix II. Codes For SMART

```
Refraction1x = Table[0, {3}, {3}];
Refraction1y = Table[0, {3}, {3}];
Refraction2x = Table[0, {3}, {3}];
Refraction2y = Table[0, {3}, {3}];
Refraction3x = Table[0, {3}, {3}];
Refraction3y = Table[0, {3}, {3}];
Samplex = Table[0, {3}, {3}];
Sampley = Table[0, {3}, {3}];
Samplez = Table[0, {3}, {3}];
Bridge = Array[b, 9];
Bridge = ReadList[C:\stress field test 2\data\2degree228x.txt]; k = 1;
Do[Refraction1x[[i, j]] = 254/24 * Bridge[[k]] + x; k
Bridge = Array[b, 9];
Bridge = ReadList[C:\stress field test 2\data\2degree228y.txt]; k = 1;
Do[Refraction1y[[i, j]] = 254/24 * Bridge[[k]] + y; k = k + 1, {i, 1,3}, {j, 1,3}];
Bridge = Array[b, 9];
Bridge = ReadList[C:\stress field test 2\data\2degree206x.txt]; k = 1;
Do[Refraction2x[[i, j]] = 254/24 * Bridge[[k]] + x; k
Bridge = Array[b, 9];
Bridge = ReadList[C:\stress field test 2\data\2degree206y.txt]; k = 1;
Do[Refraction2y[[i, j]] = 254/24 * Bridge[[k]] + y; k = k + 1, {i, 1,3}, {j, 1,3}];
Bridge = Array[b, 9];
Bridge = ReadList[C:\stress field test 2\data\2degree026x.txt]; k = 1;
Do[Refraction3x[[i, j]] = 254/24 * Bridge[[k]] + x; k
Bridge = Array[b, 9];
Bridge = ReadList[C:\stress field test 2\data\2degree026y.txt]; k = 1;
Do[Refraction3y[[i, j]] = 254/24 * Bridge[[k]] + y; k = k + 1, {i, 1,3}, {j, 1,3}];
Bridge = Array[b, 9];
Bridge = ReadList[C:\Final Test\samplex.txt]; k = 1;
Do[Samplex[[i, j]] = Bridge[[k]]; k = k + 1, {i, 1,3}, {j, 1,3}];
Bridge = Array[b, 9];
Bridge = ReadList[C:\Final Test\sampley.txt]; k = 1;
Do[Sampley[[i, j]] = Bridge[[k]]; k = k + 1, {i, 1,3}, {j, 1,3}];
Bridge = Array[b, 9];
Bridge = ReadList[C:\Final Test\samplez.txt]; k = 1;
Do[Samplez[[i, j]] = Bridge[[k]]; k = k + 1, {i, 1,3}, {j, 1,3}];
IncidentBeam = {0,0,1};
uxxmatr = Table[0, {3}, {3}]; uxymatr = Table[0, {3}, {3}];
```

uxzmatr = Table[0, {3}, {3}]; uyxmatr = Table[0, {3}, {3}];
uyymatr = Table[0, {3}, {3}]; uyzmatr = Table[0, {3}, {3}];
uzxmatr = Table[0, {3}, {3}]; uzymatr = Table[0, {3}, {3}];
uzzmatr = Table[0, {3}, {3}]; exxmatr = Table[0, {3}, {3}];
exymatr = Table[0, {3}, {3}]; exzmatr = Table[0, {3}, {3}];
eyxmatr = Table[0, {3}, {3}]; eyymatr = Table[0, {3}, {3}];
eyzmatr = Table[0, {3}, {3}]; ezxmatr = Table[0, {3}, {3}];
ezymatr = Table[0, {3}, {3}]; ezzmatr = Table[0, {3}, {3}];

N01

$$= \begin{pmatrix} \mathrm{Cos}[c] & -\mathrm{Sin}[c] & 0 \\ \mathrm{Sin}[c] & \mathrm{Cos}[c] & 0 \\ 0 & 0 & 1 \end{pmatrix} \cdot \begin{pmatrix} \mathrm{Cos}[b] & 0 & \mathrm{Sin}[b] \\ 0 & 1 & 0 \\ -\mathrm{Sin}[b] & 0 & \mathrm{Cos}[b] \end{pmatrix} \cdot \begin{pmatrix} 1 & 0 & 0 \\ 0 & \mathrm{Cos}[a] & -\mathrm{Sin}[a] \\ 0 & \mathrm{Sin}[a] & \mathrm{Cos}[a] \end{pmatrix} \cdot \{0,8,-2^{1.5}\};$$

N01 = Normalize[N01];
N02

$$= \begin{pmatrix} \mathrm{Cos}[c] & -\mathrm{Sin}[c] & 0 \\ \mathrm{Sin}[c] & \mathrm{Cos}[c] & 0 \\ 0 & 0 & 1 \end{pmatrix} \cdot \begin{pmatrix} \mathrm{Cos}[b] & 0 & \mathrm{Sin}[b] \\ 0 & 1 & 0 \\ -\mathrm{Sin}[b] & 0 & \mathrm{Cos}[b] \end{pmatrix} \cdot \begin{pmatrix} 1 & 0 & 0 \\ 0 & \mathrm{Cos}[a] & -\mathrm{Sin}[a] \\ 0 & \mathrm{Sin}[a] & \mathrm{Cos}[a] \end{pmatrix} \cdot \{-2\text{\textasciicircum}0.5,6,-2\text{\textasciicircum}0.5\};$$

N02 = Normalize[N02];
N03

$$= \begin{pmatrix} \mathrm{Cos}[c] & -\mathrm{Sin}[c] & 0 \\ \mathrm{Sin}[c] & \mathrm{Cos}[c] & 0 \\ 0 & 0 & 1 \end{pmatrix} \cdot \begin{pmatrix} \mathrm{Cos}[b] & 0 & \mathrm{Sin}[b] \\ 0 & 1 & 0 \\ -\mathrm{Sin}[b] & 0 & \mathrm{Cos}[b] \end{pmatrix} \cdot \begin{pmatrix} 1 & 0 & 0 \\ 0 & \mathrm{Cos}[a] & -\mathrm{Sin}[a] \\ 0 & \mathrm{Sin}[a] & \mathrm{Cos}[a] \end{pmatrix} \cdot \{2\text{\textasciicircum}0.5,6,-2\text{\textasciicircum}0.5\};$$

N03 = Normalize[N03];
Sample = Table[0, {3}, {3}, {3}];
For[$i = 1, i \le 3, i + +$,
For[$j = 1, j \le 3, j + +$,

Sample$[[i, j, 1]]$

$$= \left(\mathrm{Samplex}[[i, j]] - \mathrm{Samplex}[[2,2]]\right) * \mathrm{Cos}[\beta]$$

$$- \left(\mathrm{Samplez}[[i, j]] - \mathrm{Samplez}[[2,2]]\right) * \mathrm{Sin}[\beta];$$

Sample$[[i, j, 3]]$

$$= \left(\mathrm{Samplex}[[i, j]] - \mathrm{Samplex}[[2,2]]\right) * \mathrm{Sin}[\beta]$$

$$+ \left(\mathrm{Samplez}[[i, j]] - \mathrm{Samplez}[[2,2]]\right) * \mathrm{Cos}[\beta];$$

Sample[[i, j, 2]] = Sampley[[i, j]];]];
ORII

$$= \left(\begin{pmatrix} \text{Cos}[\gamma] & -\text{Sin}[\gamma] & 0 \\ \text{Sin}[\gamma] & \text{Cos}[\gamma] & 0 \\ 0 & 0 & 1 \end{pmatrix} \cdot \begin{pmatrix} \text{Cos}[b] & 0 & \text{Sin}[b] \\ 0 & 1 & 0 \\ -\text{Sin}[b] & 0 & \text{Cos}[b] \end{pmatrix} \cdot \begin{pmatrix} 1 & 0 & 0 \\ 0 & \text{Cos}[\alpha] & -\text{Sin}[\alpha] \\ 0 & \text{Sin}[\alpha] & \text{Cos}[\alpha] \end{pmatrix}\right). \text{Sample;}$$

OR = Table[0, {3}, {3}, {3}];
For[$i = 1, i \le 3, i + +$,
For[$j = 1, j \le 3, j + +$,
OR[[$i, j, 1$]] = ORII[[$i, j, 1$]]; OR[[$i, j, 2$]] = ORII[[$i, j, 2$]] − 14000; OR[[$i, j, 3$]]
      = ORII[[$i, j, 3$]] − z]];
Do[
S1 = Table[0, {3}, {3}, {3}];
For[$i = 1, i \le 3, i + +$,
For[$j = 1, j \le 3, j + +$,
S1[[$i, j, 1$]] = Refraction1x[[i, j]]; S1[[$i, j, 2$]] = Refraction1y[[i, j]]; S1[[$i, j, 3$]] = 0]];
S2 = Table[0, {3}, {3}, {3}];
For[$i = 1, i \le 3, i + +$,
For[$j = 1, j \le 3, j + +$,
S2[[$i, j, 1$]] = Refraction2x[[i, j]]; S2[[$i, j, 2$]] = Refraction2y[[i, j]]; S2[[$i, j, 3$]] = 0]];
S3 = Table[0, {3}, {3}, {3}];
For[$i = 1, i \le 3, i + +$,
For[$j = 1, j \le 3, j + +$,
S3[[$i, j, 1$]] = Refraction3x[[i, j]]; S3[[$i, j, 2$]] = Refraction3y[[i, j]]; S3[[$i, j, 3$]] = 0]];
IncidentBeam = {0,0,1};
DiffractBeam1 = Table[0, {3}, {3}, {3}];
For[$i = 1, i \le 3, i + +$,
For[$j = 1, j \le 3, j + +$,

DiffractBeam1$[[i, j]]$ = S1$[[i, j]]$ − OR$[[i, j]]$;

DiffractBeam1[[i, j]] = DiffractBeam1[[i, j]]/Norm[DiffractBeam1[[i, j]]]]];
DiffractBeam2 = Table[0, {3}, {3}, {3}];
For[$i = 1, i \le 3, i + +$,
For[$j = 1, j \le 3, j + +$,

DiffractBeam2$[[i, j]]$ = S2$[[i, j]]$ − OR$[[i, j]]$;

DiffractBeam2[[i, j]] = DiffractBeam2[[i, j]]/Norm[DiffractBeam2[[i, j]]]]];
DiffractBeam3 = Table[0, {3}, {3}, {3}];
For[$i = 1, i \le 3, i + +$,
For[$j = 1, j \le 3, j + +$,

DiffractBeam3$[[i, j]]$ = S3$[[i, j]]$ − OR$[[i, j]]$;

DiffractBeam3[[i, j]] = DiffractBeam3[[i, j]]/Norm[DiffractBeam3[[i, j]]]]];
N1 = Table[0, {3}, {3}, {3}];
For[$i = 1, i \le 3, i + +$,
For[$j = 1, j \le 3, j + +$,

```
N1[[i, j]] = DiffractBeam1[[i, j]] − IncidentBeam;

N1[[i, j]] = Normalize[N1[[i, j]]]]]];
N2 = Table[0, {3}, {3}, {3}];
For[i = 1, i ≤ 3, i + +,
For[j = 1, j ≤ 3, j + +,

N2[[i, j]] = DiffractBeam2[[i, j]] − IncidentBeam;

N2[[i, j]] = N2[[i, j]]/Norm[N2[[i, j]]]]]];
N3 = Table[0, {3}, {3}, {3}];
For[i = 1, i ≤ 3, i + +,
For[j = 1, j ≤ 3, j + +,

N3[[i, j]] = DiffractBeam3[[i, j]] − IncidentBeam;

N3[[i, j]] = N3[[i, j]]/Norm[N3[[i, j]]]]]];
Sol = NSolve[{N01[[1]] − N01[[1]] ∗ uxx − N01[[2]] ∗ uyx − N01[[3]] ∗ uzx =
          = N1[[i1, j1, 1]],

N02[[1]] − N02[[1]] ∗ uxx − N02[[2]] ∗ uyx − N02[[3]] ∗ uzx =

N03[[1]] − N03[[1]] ∗ uxx − N03[[2]] ∗ uyx − N03[[3]] ∗ uzx =
          = N3[[i1, j1, 1]]}, {uxx, uyx, uzx}];
{uxxmatr[[i1, j1]]} = uxx/. Sol; {uyxmatr[[i1, j1]]} = uyx/. Sol; {uzxmatr[[i1, j1]]}
          = uzx/. Sol;
Sol = NSolve[{N01[[2]] − N01[[1]] ∗ uxy − N01[[2]] ∗ uyy − N01[[3]] ∗ uzy =
          = N1[[i1, j1, 2]],

N02[[2]] − N02[[1]] ∗ uxy − N02[[2]] ∗ uyy − N02[[3]] ∗ uzy == N2[[i1, j1, 2]],

N03[[2]] − N03[[1]] ∗ uxy − N03[[2]] ∗ uyy − N03[[3]] ∗ uzy =
          = N3[[i1, j1, 2]]}, {uxy, uyy, uzy}];
{uxymatr[[i1, j1]]} = uxy/. Sol; {uyymatr[[i1, j1]]} = uyy/. Sol; {uzymatr[[i1, j1]]}
          = uzy/. Sol;
Sol = NSolve[{N01[[3]] − N01[[1]] ∗ uxz − N01[[2]] ∗ uyz − N01[[3]] ∗ uzz =
          = N1[[i1, j1, 3]],

N02[[3]] − N02[[1]] ∗ uxz − N02[[2]] ∗ uyz − N02[[3]] ∗ uzz =

N03[[3]] − N03[[1]] ∗ uxz − N03[[2]] ∗ uyz − N03[[3]] ∗ uzz =
          = N3[[i1, j1, 3]]}, {uxz, uyz, uzz}];
{uxzmatr[[i1, j1]]} = uxz/. Sol; {uyzmatr[[i1, j1]]} = uyz/. Sol; {uzzmatr[[i1, j1]]}
          = uzz/. Sol,
{i1,1,3}, {j1,1,3}];
Do[Extract[uxxmatr, {i, j}] >>> 9xx. txt, {i, 1,3}, {j, 1,3}];
Do[Extract[uxymatr, {i, j}] >>> 9xy. txt, {i, 1,3}, {j, 1,3}];
Do[Extract[uxzmatr, {i, j}] >>> 9xz. txt, {i, 1,3}, {j, 1,3}];
```

```
Do[Extract[uyxmatr, {i, j}] >>> 9yx. txt, {i, 1,3}, {j, 1,3}];
Do[Extract[uyymatr, {i, j}] >>> 9yy. txt, {i, 1,3}, {j, 1,3}];
Do[Extract[uyzmatr, {i, j}] >>> 9yz. txt, {i, 1,3}, {j, 1,3}];
Do[Extract[uzxmatr, {i, j}] >>> 9zx. txt, {i, 1,3}, {j, 1,3}];
Do[Extract[uzymatr, {i, j}] >>> 9zy. txt, {i, 1,3}, {j, 1,3}];
Do[Extract[uzzmatr, {i, j}] >>> 9zz. txt, {i, 1,3}, {j, 1,3}];
i = 9;
xx = Array[xx, 6];
xx
= ReadList[D:\Documents and Settings\Tianyi Zhou\My Documents\9xx.txt];
yy = Array[yy, 6];
yy
= ReadList[D:\Documents and Settings\Tianyi Zhou\My Documents\9yy.txt];
zz = Array[zz, 6];
zz = ReadList["D:\Documents and Settings\Tianyi Zhou\My Documents\9zz. txt"];
xy = Array[xy, 6];
xy
= ReadList[D:\Documents and Settings\Tianyi Zhou\My Documents\9xy.txt];
yz = Array[yz, 6];
yz
= ReadList[D:\Documents and Settings\Tianyi Zhou\My Documents\9yz.txt];
xz = Array[xz, 6];
xz = ReadList["D:\Documents and Settings\Tianyi Zhou\My Documents\9xz. txt"];
yx = Array[yx, 6];
yx = ReadList[D:\Documents and Settings\Tianyi Zhou\My Documents\9yx.txt];
zy = Array[yx, 6];
zy
= ReadList[D:\Documents and Settings\Tianyi Zhou\My Documents\9zy.txt];
zx = Array[yx, 6];
zx = ReadList["D:\Documents and Settings\Tianyi Zhou\My Documents\9zx. txt"];
strain = Table[0, {3}, {3}];
```

$$\text{strain}[[1,1]] = xx[[i]]; \text{strain}[[1,2]] = xy[[i]]; \text{strain}[[1,3]] = xz[[i]]; \text{strain}[[2,1]]$$

$$= yx[[i]];$$

$$\text{strain}[[2,2]] = yy[[i]]; \text{strain}[[2,3]] = yz[[i]]; \text{strain}[[3,1]] = zx[[i]];$$

$$\text{strain}[[3,2]] = zy[[i]]; \text{strain}[[3,3]] = zz[[i]];$$

$$A = \{\{\frac{1}{\sqrt{2}}, 0, \frac{-1}{\sqrt{2}}\}, \{-\frac{1}{\sqrt{2}}, 0, -\frac{1}{\sqrt{2}}\}, \{0,1,0\}\};$$

```
stiffness = Table[0, {i, 1,3}, {j, 1,3}, {k, 1,3}, {l, 1,3}];
stiffness[[1]][[1]][[1]][[1]] = stiffness[[2]][[2]][[2]][[2]] = stiffness[[3]][[3]][[3]][[3]]
              = 165.7;
```

stiffness$[[1]][[1]][[2]][[2]]$ = stiffness$[[2]][[2]][[3]][[3]]$ = stiffness$[[3]][[3]][[1]][[1]]$

$$= \text{stiffness}[[2]][[2]][[1]][[1]] = \text{stiffness}[[3]][[3]][[2]][[2]]$$

$$= \text{stiffness}[[1]][[1]][[3]][[3]] = 63.9;$$

stiffness$[[3]][[2]][[3]][[2]]$ = stiffness$[[3]][[2]][[2]][[3]]$ = stiffness$[[2]][[3]][[3]][[2]]$
$\quad\quad\quad$ = stiffness$[[2]][[3]][[2]][[3]]$ = stiffness$[[3]][[1]][[3]][[1]]$
$\quad\quad\quad$ = stiffness$[[3]][[1]][[1]][[3]]$ = stiffness$[[1]][[3]][[3]][[1]]$
$\quad\quad\quad$ = stiffness$[[1]][[3]][[1]][[3]]$ = stiffness$[[2]][[1]][[2]][[1]]$
$\quad\quad\quad$ = stiffness$[[2]][[1]][[1]][[2]]$ = stiffness$[[1]][[2]][[2]][[1]]$
$\quad\quad\quad$ = stiffness$[[1]][[2]][[1]][[2]]$ = 79.6;

Cstiff = Table[Sum[$A[[m]][[i]]A[[n]][[j]]A[[o]][[k]]A[[p]][[l]]$stiffness$[[i]][[j]][[k]][[l]]$,
$\{i,1,3\},\{j,1,3\},\{k,1,3\},\{l,1,3\}],\{m,1,3\},\{n,1,3\},\{o,1,3\},\{p,1,3\}];$

c11 = Cstiff$[[1,1,1,1]]$; c22 = Cstiff$[[2,2,2,2]]$; c33 = Cstiff$[[3,3,3,3]]$;

c44 = Cstiff$[[2,3,2,3]]$; c55 = Cstiff$[[1,3,1,3]]$; c66 = Cstiff$[[2,1,2,1]]$;

c12 = Cstiff$[[1,1,2,2]]$; c13 = Cstiff$[[1,1,3,3]]$; c23 = Cstiff$[[2,2,3,3]]$;
Do[

exxmatr$[[i1,j1]]$ = uxxmatr$[[i1,j1]]$;

exymatr$[[i1,j1]]$ = 1/2 (uxymatr$[[i1,j1]]$ + uyxmatr$[[i1,j1]]$);

exzmatr$[[i1,j1]]$ = 1/2 (uxzmatr$[[i1,j1]]$ + uzxmatr$[[i1,j1]]$);

eyymatr$[[i1,j1]]$ = uyymatr$[[i1,j1]]$;

eyzmatr$[[i1,j1]]$ = 1/2 (uyzmatr$[[i1,j1]]$ + uzymatr$[[i1,j1]]$);

ezzmatr$[[i1,j1]]$ = uzzmatr$[[i1,j1]]$,
$\{i1,1,3\},\{j1,1,3\}];$
sigmaxx = c11 * exxmatr + c12 * eyymatr + c13 * ezzmatr
sigmayy = c12 * exxmatr + c22 * eyymatr + c23 * ezzmatr
sigmazz = c13 * exxmatr + c23 * eyymatr + c33 * ezzmatr
sigmayz = c44 * 2 * eyzmatrsigmaxz = c55 * 2 * exzmatr
sigmaxy = c66 * 2 * exymatr
stress = Array[stress, 6];

stress$[[1]]$ = sigmaxx; stress$[[2]]$ = sigmayy; stress$[[3]]$ = sigmazz;

stress$[[4]]$ = sigmaxy; stress$[[5]]$ = sigmaxz; stress$[[6]]$ = sigmayz;
Do[Extract[stress, $\{i\}$] >>> 9g9. txt, $\{i,1,6\}];$
$k = 9;$

Pointx = Array[pointx, 5]; Bridge = Array[bridge, 5];

Bridge = ReadList["C:\Final Test\x. txt"]; Do[Pointx[[i]] = Bridge[[i]], {i, 1,5}]

Pointy = Array[pointy, 6];

Bridge = Array[bridge, 9];

Bridge = ReadList[C:\Final Test\average stress\2yy.txt];

Pointy[[1]] = Bridge[[k]];

Bridge = Array[bridge, 9];

Bridge = ReadList[C:\Final Test\average stress\3yy.txt];

Pointy[[2]] = Bridge[[k]];

Bridge = Array[bridge, 9];

Bridge = ReadList[C:\Final Test\average stress\4yy.txt];

Pointy[[3]] = Bridge[[k]];

Bridge = Array[bridge, 9];

Bridge = ReadList[C:\Final Test\average stress\47yy.txt];

Pointy[[4]] = Bridge[[k]];

Bridge = Array[bridge, 9];

Bridge = ReadList[C:\Final Test\average stress\8yy.txt];

Pointy[[5]] = Bridge[[k]];

data = Table[0, {5}, {2}];

Do[data[[i, 1]] = Pointx[[i]], {i, 1,5}]; Do[data[[i, 2]] = Pointy[[i]], {i, 1,5}]; data

NSolve[

{Pointy[[1]] =

$$= 1/\text{Pointx}[[1]] * (\frac{a0}{a3 + 1/\text{Pointx}[[1]]} + \frac{a1}{(a3 + 1/\text{Pointx}[[1]])^2}$$

$$+ \frac{2 * a2}{(a3 + 1/\text{Pointx}[[1]])^3}),$$

Pointy[[2]] == 1/Pointx[[2]]

$$* \left(\frac{a0}{a3 + 1/\text{Pointx}[[2]]} + \frac{a1}{(a3 + 1/\text{Pointx}[[2]])^2} + \frac{2 * a2}{(a3 + 1/\text{Pointx}[[2]])^3}\right),$$

Pointy[[3]] == 1/Pointx[[3]]

$$* \left(\frac{a0}{a3 + 1/\text{Pointx}[[3]]} + \frac{a1}{(a3 + 1/\text{Pointx}[[3]])^2} + \frac{2 * a2}{(a3 + 1/\text{Pointx}[[3]])^3}\right),$$

$$\text{Pointy}[[4]] == 1/\text{Pointx}[[4]] * \left(\frac{a0}{a3 + 1/\text{Pointx}[[4]]} + \frac{a1}{(a3 + 1/\text{Pointx}[[4]])\wedge 2}\right.$$
$$\left. + \frac{2 * a2}{(a3 + 1/\text{Pointx}[[4]])\wedge 3}\right)\}, \{a0, a1, a2, a3\}]$$

$$y[\text{x}_-] = 1/x * \left(\frac{a0}{a3 + 1/x} + \frac{a1}{(a3 + 1/x)^2} + \frac{2 * a2}{(a3 + 1/x)^3}\right)$$

curve1 $= (1/s) * (y[x]/. x \to 1/s)$; curve1;

sigmaxx $=$ InverseLaplaceTransform[curve1, s, t]

Plot[$y[x]$, $\{x, 80,120\}$, Mesh $\to$ True, AxesLabel $\to$ {depth, stress}, PlotStyle
$\to$ Thick, GridLines $\to$ Automatic, Frame $\to$ True]

Plot[sigmaxx, $\{t, 80,120\}$, Mesh $\to$ True, AxesLabel $\to$ {depth, stress}, PlotStyle
$\to$ Thick, GridLines $\to$ Automatic, Frame $\to$ True]

Appendix III. Principle of Raman Spectroscopy Residue Stress Measurement
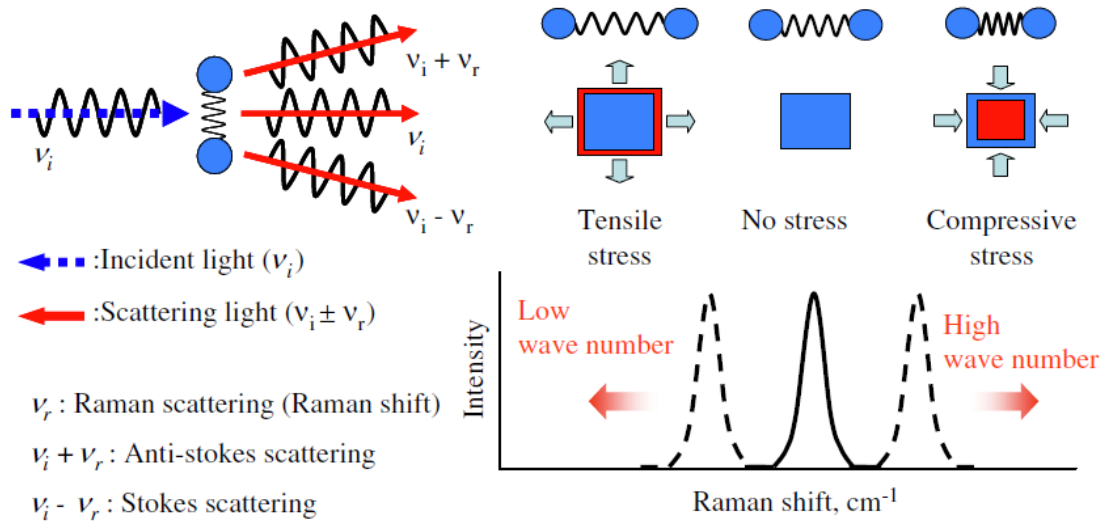
Shift = sum of stress components

$$\text{Strain}(\varepsilon) = \frac{a - a_{Si}}{a_{Si}}$$

Biaxial Stress:

$$\sigma_{XX} + \sigma_{YY} = -\frac{Shift(cm^{-1})}{1.92 cm^{-1}/GPa}$$